

# 1 Modeling tabular icebergs coupled to an ocean model

2 **A. A. Stern<sup>1</sup>, A. Adcroft<sup>1</sup>, O. Sergienko<sup>1</sup>, G. Marques<sup>1</sup>, R. Hallberg<sup>1</sup>**

3 <sup>1</sup>Geophysical Fluid Dynamics Laboratory, Princeton University  
4 <sup>1</sup>201 Forrestal Rd, Princeton, NJ 08540, USA

## 5 **Key Points:**

- 6
- 7
- 8
- 9
- 10
- A novel modeling framework is developed to explicitly model large tabular icebergs submerged in the ocean.
  - Tabular icebergs are constructed out of Lagrangian elements that drift in the ocean, and are held together by numerical bonds.
  - Breaking the numerical bonds allows us to model iceberg breakup and calving.

11 **Abstract**

12 Large tabular icebergs calved from Antarctic ice shelves have long lifetime (due to their  
 13 large size), during which they drift across large distances, altering regional ocean circulation,  
 14 bottom-water formation, sea-ice formation and biological primary productivity in  
 15 the icebergs' vicinity. However, despite their importance, the current generation of ocean  
 16 circulation models is unable to represent large tabular icebergs. In this study we develop  
 17 a novel framework to model large tabular icebergs submerged in the ocean. In this frame-  
 18 work, tabular icebergs are composed of Lagrangian elements that drift in the ocean, and  
 19 are held together and interact with each other via bonds. A break of these bonds allows  
 20 the model to emulate calving events (i.e. detachment of a tabular iceberg from an ice  
 21 shelf), splitting of large tabular icebergs, and breaking off smaller pieces from the ice-  
 22 bergs. Idealized simulations of calving of a tabular iceberg, its drifting and splitting in two  
 23 smaller tabular icebergs demonstrate capabilities of the developed framework.

24 **1 Introduction**

25 Large tabular icebergs - pieces of floating ice with horizontal dimensions substan-  
 26 tially larger than the vertical dimension - calve infrequently (~ every forty-fifty years)  
 27 from Antarctic or Greenlandic ice shelves [?]. Observational estimates suggest that over  
 28 the past 30 years approximately half of Antarctic ice-shelf decay is due to iceberg calving,  
 29 while the other half occurs through ice-shelf melting [Depoorter et al , 2013; Rignot et al  
 30 , 2013]. The infrequent tabular icebergs (horizontal extent larger than 5 km) account for  
 31 more than 90% of the Southern Hemisphere iceberg mass [Tournadre et al , 2016].

32 After calving, icebergs slowly drift away from their origins, often becoming stuck in  
 33 sea ice, or grounding on bathymetric highs along the Antarctic coast [Lichéy and Hellmer  
 34 , 2001; Dowdeswell and Bamber , 2007]. Large tabular icebergs extend deep into the wa-  
 35 ter column, and have the potential to disrupt ocean circulation patterns for months or even  
 36 years after calving [Robinson et al , 2012; Stern et al , 2015]. The freshwater flux from  
 37 iceberg melt impacts ocean hydrography around the iceberg, influencing sea-ice produc-  
 38 tion and bottom-water formation [Arrigo et al , 2002; Robinson et al , 2012; Nicholls et  
 39 al , 2009; Fogwill et al , 2016]. Because of their large size, the tabular icebergs have long  
 40 lifetime during which they drift over long distances injecting meltwater along the way and  
 41 impacting the Southern Ocean state (e.g. hydrography, sea ice conditions, etc.) far away  
 42 from their calving origins [Stern et al , 2016]. Meltwater injection (and the accompanying  
 43 upwelling) from icebergs can also influence biological productivity by bringing nutrients  
 44 to the surface ocean or changing sea ice conditions [Arrigo et al , 2002; Vernet et al ,  
 45 2012; Biddle et al , 2015]. The increased productivity associated with free-floating tabu-  
 46 lar icebergs has been linked with local increases in ocean carbon uptake, potentially large  
 47 enough to be a significant fraction of the Southern Ocean carbon sequestration [Smith et  
 48 al , 2007].

49 In recent years, there has been an increased interest in iceberg drift and decay. This  
 50 surge of interest has been driven by (i) the need to understand polar freshwater cycles  
 51 in order to create realistic climate forecasts and sea level projections [Silva et al , 2006;  
 52 Shepherd and Wingham , 2007; Rignot et al , 2013]; and (ii) the increased navigation and  
 53 exploration activities in high-latitudes iceberg-filled waters in the Arctic [Pizzolato et al  
 54 , 2012; Unger , 2014; Henderson and Loe , 2016]. The increased interest in icebergs has  
 55 led to the development of numerical models of iceberg drift and decay [Mountain , 1980;  
 56 Bigg et al , 1997; Gladstone et al , 2001; Kubat et al , 2005], some of which have been  
 57 included in global General Circulation Models [Martin and Adcroft , 2010; Marsh et al  
 58 , 2015]. These iceberg drift models treat icebergs as Lagrangian point particles, which  
 59 are advected by the flow, and melt according to certain parameterizations for icebergs  
 60 melt. Since icebergs are treated as point particles, iceberg drift models are mostly suitable  
 61 for modeling icebergs smaller than an ocean grid cell. Consequently, these models have

mostly been used to represent icebergs smaller than 3.5 km on a global scale [Jongma et al , 2009; Martin and Adcroft , 2010; Marsh et al , 2015].

Point-particle iceberg drift models are less suitable for modeling larger tabular icebergs, where the size and structure of the iceberg may be an important feature in determining their drift and decay [Stern et al , 2016]. They also are not suitable for studying the local effects that icebergs have on the surrounding ocean, or the small scale processes that influence iceberg melt and decay [Wagner et al , 2014; Stern et al , 2015]. For these reasons, tabular icebergs are currently not represented in the iceberg drift models used as components of climate models, despite accounting for the vast majority of the total Southern Hemisphere iceberg mass [Tournadre et al , 2016]. Point-particle iceberg models also do not have any representation of iceberg breakup and calving, which is known to be an important iceberg decay mechanism.

The goal of this study is to develop a new framework to model all kinds of icebergs where tabular icebergs are explicitly resolved. Our new representation of icebergs aims to include the following key properties: (i) icebergs should be able to travel large distances within the ocean, (ii) icebergs should melt and decay as they drift in the ocean, (iii) icebergs should behave as if they have finite extent (in order to model local effects that icebergs have on the surrounding ocean), and (iv) tabular icebergs should be able to break away from ice shelves or break into smaller pieces. Properties (i) and (ii) are common to point-particle icebergs models, while properties (iii) and (iv) are new to the framework developed in this study.

In order to allow icebergs to travel large distance, it is natural to model the icebergs in a Lagrangian framework (as in the point particle iceberg drift models described above). In our model we therefore represent icebergs using Lagrangian elements. However, in the new framework, icebergs are no longer treated as point particles that interact with the ocean at a point location, but rather icebergs are given structure, so that they interact with the ocean across multiple ocean grid cells. To do this, we represent tabular icebergs as a collection of many Lagrangian elements with finite extent which are ‘bonded’ together by numerical bonds. The numerical bonds hold the ice elements together and allow a collection of elements to move as a unit (see schematic in Figure 1). An advantage of this approach is that we can break the numerical bonds to simulate an iceberg detaching from an ice shelf (e.g.: Figure 2 and 3) or an iceberg breaking up into smaller pieces.

The manuscript is organized as follows. Section 2 gives a description of many of the key aspects of the model. Since this model is a new approach to modeling icebergs, we present many of the technical aspects of the model. In section 3 and 4, we demonstrate the capabilities of the model by simulating a tabular iceberg detaching from an idealized ice shelf. In a further simulations we sever some numerical bonds within the tabular iceberg to demonstrate iceberg breaking.

## 2 Model description

The Lagrangian Bonded Iceberg Model (LBIM) is a Lagrangian particle-based model in that the objects of the model are Lagrangian elements. Each element represents a column of ice that is floating in the ocean, and has a position, velocity, mass, and a set of dimensions, which can evolve in time. The motion of each element is determined by a momentum equation which is solved in the (Lagrangian) reference frame of the element. The elements experience oceanic and atmospheric forces, which are either prescribed, or computed by coupling the LBIM to an ocean/atmosphere model. The LBIM elements also interact with one another and can be bonded together to form larger structures.

In different contexts, the LBIM elements can be thought to represent individual icebergs, sea ice flows, or, when the elements are bonded together, they can represent larger structures such as tabular icebergs or ice shelves.

The ice elements in the LBIM are given finite extent by assigning to each element a finite surface area and shape, and allowing each element to interact with other elements when the boundaries of the elements overlap. The finite extent of the elements is felt by the ocean by distributing the elements' weight and melt fluxes over multiple ocean grid cells in a way which is consistent with the shape of the ice elements. To simplify the model, we only use ice elements with hexagonal surface area. In order represent icebergs with other shapes, we introduce numerical bonds which allow multiple ice elements to be bonded together to form larger structures. The numerical bonds hold the ice elements together and allow a collection of elements to move as a unit. The angular momentum of the elements is not modeled explicitly; instead rotational motion of larger structures emerge as a consequence of bond orientation and collective motion.

The LBIM is developed on the code base of an existing iceberg drift model [Martin and Adcroft , 2010; Stern et al , 2016]. When run with the correct set of runtime flags, the model runs as a traditional iceberg drift model.

## 2.1 Equations of motion

The elements drift in the ocean, in response to atmosphere, ocean and sea-ice drag forces, as well as the Coriolis force and a force due to the sea surface slope. When these ice elements move alone (without interactions with other elements), they can be thought of as representing individual (or clusters of) small icebergs, and follow the same equations described in the iceberg drift model of Martin and Adcroft [2010] (based on the equations outlined in Bigg et al [1997] and Gladstone et al [2001]).

In addition to the external forces, the elements in the LBIM experience interactive forces due to the presence of other elements. Two types of interactive forces are included between elements. The first force is a repulsive force which is applied to elements to prevent them from overlapping the boundaries of the neighboring elements. The second interactive force is a force due to numerical ‘bonds’, and is only applied if two elements are labelled as ‘bonded’. When two elements are bonded, each element feels an attractive force that prevents the elements from moving too far apart from one another.

The momentum equation for each element is given by

$$M \frac{D\vec{u}}{Dt} = \vec{F}_A + \vec{F}_W + \vec{F}_R + \vec{F}_C + \vec{F}_{SS} + \vec{F}_{SI} + \vec{F}_{IA}, \quad (1)$$

where  $\frac{D}{Dt}$  is the total (Lagrangian) derivative,  $M$  is the mass of the element,  $\vec{u}$  is the velocity of the element, and the terms on the right hand side give the forces on the element due to air drag ( $\vec{F}_A$ ), water drag ( $\vec{F}_W$ ), sea ice drag ( $\vec{F}_{SI}$ ), Coriolis force ( $\vec{F}_C$ ), wave radiation force ( $\vec{F}_R$ ), sea surface slope ( $\vec{F}_{SS}$ ), and interactions with other elements ( $\vec{F}_{IA}$ ). The environmental forces are the same as those presented in Martin and Adcroft [2010], and are provided for completeness in Appendix A. The details of the interactive forces are provided in below.

## 2.2 Interactive Forces

The interactive forces in the LBIM model are used to (i) prevent the ice elements from overlapping and (ii) to connect multiple ice elements so that they move together as a rigid body. Modeling the collisions and movements of rigid objects precisely, requires very small time steps and precise collision detection algorithms, which are very time consuming. Models using these methods are typically only run for a few days or even a few seconds, and are used to study rapid processes like crack formation or ridging [?Bassis and Jacobs , 2013; ?]. The tabular iceberg framework presented in this study is developed in order to be used in general circulation models used for climate, and therefore must be run for many years. In order to gain the required computational efficiency, we relax the requirement that icebergs must be perfectly rigid and that ice elements can not overlap.

Instead, we model the interactive forces between icebergs using damped elastic forces, which can be calculated more rapidly.

The total interactive force on an element is calculated by adding together the interactions with all other elements, such that the interactive force on element  $i$ ,  $(\vec{F}_{IA})_i$  is given by:

$$(\vec{F}_{IA})_i = \sum_{j \neq i} (\vec{F}_{IA})_{ij}, \quad (2)$$

where  $(\vec{F}_{IA})_{ij}$  is the force on element  $i$  by element  $j$ . Both bonded and repulsive interactions are modeled using elastic stresses with frictional damping. The elastic component of the force is a function of the distance between the two elements, while the frictional damping force depends on the relative velocity of the two elements.

To describe the forces between two elements, we begin by introducing some notation. Let  $\vec{x}_i$ ,  $\vec{x}_j$  be the positions of elements  $i$  and  $j$ . The distance between elements  $i$  and  $j$  is

$$d_{ij} = |\vec{x}_i - \vec{x}_j|. \quad (3)$$

When calculating the interactive forces between elements, the elements are assumed to be circular. We define the interaction diameter of an element by

$$D_i = 2 \sqrt{\frac{A_i}{\pi}}, \quad (4)$$

where  $A_i$  is the planar surface area of element  $i$ . Using this, we define the critical interactive length scale,

$$L_{ij} = \frac{D_i + D_j}{2}, \quad (5)$$

which governs interactions between elements  $i$  and  $j$ . Repulsive forces are only applied when  $d_{i,j} < L_{i,j}$ , while for  $d_{i,j} > L_{i,j}$  attractive bonded forces are applied when a bond exists between element  $i$  and  $j$ .

To aid in notation, we define a bond matrix  $B_{ij}$  such that  $B_{ij} = 1$  if elements  $i$  and  $j$  are bonded together and  $B_{ij} = 0$  otherwise. Using this notation, the interactive force  $(\vec{F}_{IA})_{ij}$  on an element  $i$  by an element  $j$  is given by

$$(\vec{F}_{IA})_{ij} = \begin{cases} (\vec{F}_e)_{ij} + (\vec{F}_d)_{ij} & \text{if } d_{ij} \leq L_{ij} \\ (\vec{F}_e)_{ij} + (\vec{F}_d)_{ij} & \text{if } d_{ij} > L_{ij} \text{ and } B_{ij} = 1 \\ 0 & \text{if } d_{ij} > L_{ij} \text{ and } B_{ij} = 0. \end{cases} \quad (6)$$

$(\vec{F}_e)_{ij}$  and  $(\vec{F}_d)_{ij}$  are the elastic and frictional damping components of the interactive force between elements  $i$  and  $j$ . The elastic force  $(\vec{F}_e)_{ij}$  between elements is given by

$$(\vec{F}_e)_{ij} = -\kappa_e (d_{i,j} - L_{i,j}) T_{i,j} \vec{r}_{ij}, \quad (7)$$

where  $\vec{r}_{ij} = \frac{(\vec{x}_i - \vec{x}_j)}{|\vec{x}_i - \vec{x}_j|}$  is the directional unit vector between the position of element  $i$  and  $j$ ,  $\kappa_e$  is the spring constant, and  $T_{i,j}$  is the minimum of the thickness of elements  $i$ ,  $j$ . The interactive forces obey Newton's 3rd Law (i.e.:  $(\vec{F}_{IA})_{ij} = -(\vec{F}_{IA})_{ji}$ ). The minimum thickness,  $T_{i,j}$ , is preferred to the average thickness, since this means that for two bonded elements a fixed distance apart, the acceleration due to elastic forces is bounded, even when the thickness of one of the elements approaches zero. When  $d_{ij} = L_{ij}$ , the elastic forces is equal to zero, so that bonded particles will settle in an equilibrium position where elements are separated by the critical interaction length scale  $L_{i,j}$ .

The frictional damping force acts to oppose the relative velocity of the two particles. If  $\vec{r}_{ij}^\perp$  is the direction vector perpendicular to  $\vec{r}_{ij}$ , and  $P_{\vec{r}_{ij}}$  and  $P_{\vec{r}_{ij}^\perp}$  are the projection matrices that project onto  $\vec{r}_{ij}$  and  $\vec{r}_{ij}^\perp$  respectively, then the frictional damping force is given by

$$(\vec{F}_d)_{ij} = \left( -c_{r\parallel} P_{\vec{r}_{ij}} - c_{r\perp} P_{\vec{r}_{ij}^\perp} \right) \cdot (\vec{u}_i - \vec{u}_j) \quad (8)$$

195 Here  $c_{r\parallel}$  and  $c_{r\perp}$  are the drag coefficients for the damping parallel and perpendicular to  
 196  $r_{ij}$ , respectively. We set  $c_{r\parallel} = 2\sqrt{\kappa_e}$ , so that the elastic force parallel to  $\vec{r}_{ij}$  is critically  
 197 damped. The damping coefficient in the the perpendicular direction is set to  $c_{r\perp} = \frac{1}{4}c_{r\parallel}$ .  
 198 The frictional damping force perpendicular to  $\vec{r}_{ij}$  is needed to reduce motions of particles  
 199 when many particles are packed tightly together (as in the uncoupled experiments below),  
 200 and also acts to reduce the vibrations within larger bonded structures. The damping forces  
 201 are implemented using an implicit time stepping scheme, to avoid stability issues for very  
 202 small elements (details found in Appendix B).

203 Figure 4 illustrates the effectiveness of the repulsive force in an uncoupled (ice only)  
 204 simulation of the ice elements forced to drift westward into a bay. They eventually come  
 205 to rest with minimal overlap between elements. Figure 5 illustrates the effectiveness of  
 206 the numerical bonds in simulations of small icebergs (individual un-bonded elements) and  
 207 large icebergs (constructed from many ice elements bonded together) forced to drift to-  
 208 wards a convex coast line. When the tabular icebergs arrive at the coast, they bump into  
 209 the coastline and begin to rotate, influencing the paths of the other icebergs (see movie  
 210 S1 in the supplementary material). This example illustrates an advantage of using small  
 211 elements bonded together, to represent large-scale-structure and rotational motion without  
 212 explicitly accounting for the angular momentum of the elements (as discussed in Jakobsen  
 213 [2001]).

### 214 2.3 Initializing element geometry and packing

215 For purposes of packing, we assume that elements have surface areas which are  
 216 shaped as equally-sized regular hexagons (note that the elements are assumed to be cir-  
 217 cular for proposes of interactions, but are assumed to be hexagonal for packing purposes).  
 218 When packing these elements together, the hexagonal elements are initially arranged in  
 219 a staggered lattice, with each element bonded to the adjacent elements (see Figure 1). In  
 220 this arrangement, each element (away from the edges) is bonded to six other elements.  
 221 The bonds between elements form a pattern of equilateral triangles, which give the larger  
 222 structure rigidity. The circular shape of elements (used for interactions) is inscribed within  
 223 the hexagonal shape used for packing (Figure 1). The centers of adjacent elements are ini-  
 224 tially separated by a distance  $d_{i,j} = L_{i,j} = 2A_p$ , where  $A_p$  is the length the apothems of  
 225 the hexagons.

226 Some experiments were also performed using rectangular elements, arranged in a  
 227 regular (non-staggered) lattice. In this case, each element forms four bonds with adjacent  
 228 elements. However, the resultant structures were found to be much less rigid and tended  
 229 to collapse when sufficient forces was applied. For this reason, hexagonal elements are  
 230 used here.

### 231 2.4 Ocean-ice and ice-ocean coupling

232 The LBIM is coupled to the ocean model via a two-way synchronous coupling,  
 233 meaning that ocean-model fields are passed to the LBIM, and the LBIM fields are passed  
 234 back to the ocean model at every time step. Passing fields between the two models in-  
 235 volves interpolating the fields from the ocean model's Eulerian grid onto the LBIM's 'La-  
 236 grangian grid' (i.e.: onto the ice elements, Figure 1), and aggregating fields from the La-  
 237 grangian elements onto the ocean-model's Eulerian grid.

238 The coupling from the ocean model to the LBIM is straight forward: at every time  
 239 step: the ocean mixed layer temperature, salinity, velocity and sea-ice concentration are  
 240 passed from the ocean model to the LBIM, to be used in the momentum and thermo-  
 241 dynamic equations of the ice elements. Since tabular icebergs are explicitly resolved in  
 242 the ocean, it is sufficient for each element to interact with ocean mixed layer only (i.e.:  
 243 there is no need to manually embed icebergs into the ocean by integrating ocean fields

244 over the icebergs' thickness, as suggested in Merino et al [2016]). Within the LBIM, the  
 245 ocean model fields are interpolated onto the Lagrangian grid using a bilinear interpolation  
 246 scheme.

247 The coupling from the LBIM to ocean model is more complex. The LBIM influences  
 248 the ocean by: (i) applying a pressure to the ocean surface, (ii) affecting the upper  
 249 ocean by applying a no-slip boundary condition and frictional velocity beneath the ice,  
 250 and (iii) imposing heat, salt and mass fluxes on the ocean, associated with ice melting. Six  
 251 fields are passed from the LBIM to the ocean model: ice mass, ice area, frictional veloc-  
 252 ity, heat, salt, and mass fluxes. Fields from the LBIM are aggregated from the Lagrangian  
 253 elements to the Eulerian ocean grid before they are passed to the ocean model.

254 The aggregation of the LBIM fields onto the ocean grid is done in a way that is  
 255 consistent with the shape of the elements in the LBIM (see Section 2.3). Fields are 'spread'  
 256 to the ocean model grid by exactly calculating what fraction of an element's surface area  
 257 lies in a particular grid box, and dividing the field in proportion to this fraction. As an  
 258 example, consider a hexagonal element in the LBIM, which is positioned such that it in-  
 259 tersects four ocean grid cells (inset panel in Figure 1). In this situation, the mass of the el-  
 260 ement is divided between these four ocean cells in proportion to the overlap area between  
 261 the hexagonal element and the grid cell (this fraction is shown by the colors in the inset  
 262 panel in Figure 1). An advantage of this approach is that there are no jumps in pressure  
 263 as an element moves from one grid cell to another, which could trigger artificial tsunamis  
 264 within the ocean model, making the ocean model unrealistic.

265 The numerical calculation of the intersection between hexagons and the ocean grid  
 266 is simplified by dividing the hexagon into 6 equilateral triangles. This method allows for  
 267 the intersection to be found even when the hexagon is not aligned with the grid.

268 The aggregation scheme is coded with the restriction that an element's area can only  
 269 intersect a maximum of four ocean grid cells at a time. A consequence of this is that this  
 270 sets a limit on the maximum size of elements that can be represented using this model,  
 271 i.e.: the longest horizontal dimension of an ice element must be smaller than the ocean  
 272 grid spacing. Larger ice structures are constructed by bonding together smaller elements.

## 273 2.5 Melting parameterization

274 The ice elements change their mass and size due to melting, which also affects the  
 275 surrounding ocean by changing its heat and salt content. In the model, these processes are  
 276 parametrized in several ways. In this section we described the melt parametrization for  
 277 bonded, unbonded and partially bonded elements.

278 As mentioned above, ice elements which do not interact with other elements are  
 279 modeled identically to the point particle icebergs described in Martin and Adcroft [2010].  
 280 These elements melt according to three semi-empirical parametrization for melt commonly  
 281 used in previous iceberg studies [Gladstone et al , 2001; Martin and Adcroft , 2010].  
 282 Three types of iceberg melting are distinguished: basal melt,  $M_b$ , melt due to wave ero-  
 283 sion,  $M_e$  and melt due to buoyant convection,  $M_v$ .  $M_e$  and  $M_v$  are applied to the sides of  
 284 the ice element, while  $M_b$  is applied at the ice element base. The details of  $M_b$ ,  $M_v$  and  
 285  $M_e$  are given in Appendix A.

286 When multiple elements are bonded together to form larger structures, it is no longer  
 287 appropriate to use the parameterizations for melt developed for individual point-particle  
 288 icebergs. An element which is completely surrounded by other elements, is meant to rep-  
 289 resent a column of ice in the middle of a large structure, and hence will not experience  
 290 melt at its sides due to wave erosion or buoyant convection. Also, the iceberg basal melt  
 291 rate,  $M_b$  described above is based on boundary layer theory of flow past a finite plate, and  
 292 is only appropriate for basal surfaces where the distance from the leading edge is suffi-

293 ciently small [Eckert , 1950; Weeks and Campbell , 1973]. For an element in the interior  
 294 of large structures, the distance from the edge of the structure is large, and so using  $M_b$   
 295 for the basal melt is not appropriate. Instead, the basal melt,  $M_s$  is determined using the  
 296 three equation model for basal melt, which is a typical melting parametrization used be-  
 297 neath ice shelves [Holland and Jenkins , 1999].

298 When using both individual elements and bonded elements in the same simulation,  
 299 we determine which melt rate parameterizations to use based on the amount of bonds that  
 300 each element has. An element in the center of a large structure has the maximum num-  
 301 ber of bonds, while un-bonded elements has no bonds. If an element can have maximum  
 302 number of bonds  $N_{max}$ , and the number bonds that an element has is  $N_b$ , then this ele-  
 303 ment experiences the side melt and bottom melt

$$M_{side} = \frac{(N_{max} - N_b)}{N_{max}}(M_v + M_e) \quad (9)$$

304 and

$$M_{bottom} = \frac{(N_{max} - N_b)}{N_{max}}M_b + \frac{N_b}{N_{max}}M_s \quad (10)$$

305 respectively. In this way, elements with no bonds, melt like point-particle icebergs; ele-  
 306 ments at the center of large structures melt like ice shelves; and elements at the sides of  
 307 large structures have a combination of iceberg side and basal melt, and ice-shelf melt.

## 308 2.6 Algorithms and computational efficiency

309 Including interactions between elements leads to an increase in the computational  
 310 complexity of the model. In this subsection we comment on some of the algorithmic pro-  
 311 cedures that have been used to increase the computational efficiency.

### 312 2.6.1 Interactions and Bonds

313 At every time step, we calculate the force on each element due to interactions with  
 314 every other element. This involves order  $N^2$  operations (for  $N$  elements). However, since  
 315 each element only has repulsive interactions with elements that are less than one ocean  
 316 grid cell away, and each element only has bonded interactions with a small number of  
 317 other elements, we are able to reduce the number of computations.

318 This is achieved by storing the element data in an efficient way that eliminates a  
 319 search through all element pairs to check if they are close to one another or are bonded  
 320 with one another. The data storage system is organized as follows: pointers to the memory  
 321 structures containing each element are stored in linked list data structures, which allow  
 322 elements to be added and removed from the lists easily without restructuring the entire  
 323 list. Instead of using one list for all the elements on a processor (as was done in the orig-  
 324 inal code [Martin and Adcroft , 2010]), we use a separate linked list for each ocean grid  
 325 cell. When an element moves between ocean grid cells, it is removed from its original list  
 326 and added to the list corresponding to its new ocean grid cell. Since the area of elements  
 327 has to be smaller than the area of an ocean grid cell, the critical interaction length scale  
 328 (equation 5) is less than the size of a grid cell. This means that elements only experience  
 329 repulsive forces with other elements in the same ocean grid cell, or in one of the 8 adjac-  
 330 ent cells. At each time step and for each element  $i$ , the code traverses these linked lists  
 331 of the 9 surrounding grid cells, and applies a repulsive force if  $d_{i,j} < L_{ij}$  (whether the  
 332 elements are bonded or not). Limiting the possible repulsive interactions to elements in  
 333 these 9 linked lists substantially reduces the computational time needed to calculate the  
 334 total interactive forces.

335 The attractive force is computed in a following way. Each bond is assigned a piece  
 336 of memory. Each ice element contains a linked list of each of its bonds (typically up to

337 six bonds per element). At every time step, the code traverses the lists of bonded ele-  
 338 ments, and adds an attractive bonded force corresponding to these bonds if  $d_{i,j} > L_{ij}$   
 339 (the repulsive bonded force to be applied when  $d_{i,j} < L_{ij}$  is already accounted for by the  
 340 procedure outlined in the previous paragraph). Having a list of bonds stored with each el-  
 341 ement reduces the computations need for bonded interactions from order  $N^2$  to order N.  
 342 Computing attractive forces separately from the other forces allows us to avoid checking  
 343 whether two elements are bonded, which further increases the computational efficiency.

### 344 **2.6.2 Parallelization and halos**

345 The LBIM runs on multiple processors in parallel (using the same grid decomposi-  
 346 tion as the ocean model). When elements move from an ocean cell on one processor to  
 347 an ocean cell on a second processor, the memory has to be passed from one processor the  
 348 next, added and removed to the appropriate lists and the memory has to be allocated and  
 349 deallocated correctly. Element interactions across the edge of processors are handled using  
 350 computational halos. A computational halo is a copy of the edge of a one processor which  
 351 is appended to the edge of a second processor, so that the first processor can interact with  
 352 the second processor during a time step. Before each time step, elements at the edges of  
 353 each processor are copied onto the halos of adjacent processors so that they can be used  
 354 in calculating the interactive forces. After each time step, these halos are removed, and  
 355 the process is repeated. These halo updates are one of the most computationally expensive  
 356 parts of the LBIM. Details of how the bonds are broken and reconnected across processor  
 357 boundaries are provided in Appendix C.

### 358 **2.6.3 Time stepping**

359 The elements in the LBIM are advected using a semi-implicit velocity Verlet time-  
 360 stepping scheme. The velocity Verlet time stepping scheme is commonly used in discrete  
 361 element models in video games because it is computational efficient and has desirable  
 362 stability properties [Jakobsen , 2001]. This time stepping scheme was preferred to the  
 363 Runge-Kutta 4, which was used in the iceberg model of Martin and Adcroft [2010] since  
 364 the Verlet time stepping only requires one calculation of the interactive forces once per  
 365 time step (while the Runge-Kutta scheme requires the interactive forces to be calculated  
 366 four times). Since the calculation of the interactive forces is one of the most computa-  
 367 tionally expensive part of the algorithm, the Verlet scheme leads to a significant increase  
 368 in the computational efficiency of the model. We note that the Verlet scheme used in the  
 369 LBIM contains a modification of the original (fully explicit) velocity Verlet time stepping  
 370 scheme in that damping terms are treated implicitly (which increases the numerical stabil-  
 371 ity). The details of this time stepping scheme are outline in Appendix B.

## 372 **3 Experiment Setup**

373 The introduction of Lagrangian elements, numerical bonds and interpolation schemes  
 374 between the Eulerian and Lagrangian grids (discussed in Section 2) means that we now  
 375 have the tools to model large tabular icebergs submerged in the ocean. We demonstrate  
 376 this capability by simulating a tabular iceberg drifting away from an ice shelf in idealized  
 377 setting.

### 378 **3.1 Model configuration**

379 We use the geometric setup of the Marine Ice Ocean Modeling Inter-comparison  
 380 Project (MISOMIP) [Asay-Davis et al , 2016]. The configuration consists of an idealized  
 381 ice shelf in a rectangular domain. The domain is  $L_x = 80$  km wide and  $L_y = 480$  km  
 382 long, and contains an ice shelf which is grounded on the south side of the domain and  
 383 has an ice front at  $y=650$  km. The ice thickness and bottom topography of this setup are

384 shown in Figure 6a and 6b respectively, with the grounding line position drawn in for reference.  
 385 The configuration is the same as that of the Ocean0 setup in the MISOMIP, with a  
 386 few minor changes to the ice-shelf geometry (see Supplementary Material for details).

### 387 3.2 Initializing Lagrangian elements:

388 The idealized ice shelf is constructed out of Lagrangian ice elements. Ice elements  
 389 are hexagonal and are arranged in a regular staggered lattice (as discussed in Section 2.3).  
 390 The sides of the hexagons are initialized with length  $S = 0.98$  km. Gaps along the bound-  
 391 aries are filled in using smaller elements so that the total ice-shelf area is preserved. The  
 392 initial mass of the ice elements is determined by a preprocessing inversion performed be-  
 393 fore the model is run. When the model runs, the mass of elements is aggregated from the  
 394 Lagrangian grid onto the Eulerian ocean grid (see Section 2.3), and is used to find the sur-  
 395 face pressure or ice draft (part of an ice column submerged into the ocean). The ice draft  
 396 calculated without the aggregation (treating elements as point masses) contains large grid  
 397 artifacts (Figures 6c). These grid artifacts are much reduced after the mass-spreading ag-  
 398 gregation is used (Figure 6b).

### 399 3.3 Ocean model setup

400 The LBIM is coupled to the MOM6 ocean model [Hallberg et al , 2013]. The ocean  
 401 model configuration uses a vertical coordinate system which is a hybrid between a sigma-  
 402 level and a z-level coordinate. In particular, model layers deform underneath the ice shelf  
 403 as they would in a sigma-coordinate model, but collapse to zero thickness when they in-  
 404 tersect with bottom topography, as they would in a z-level model. The coordinate system  
 405 was achieved using ALE regridding-remapping scheme [White et al , 2009]. The model  
 406 uses a horizontal resolution of 2 km, and 72 vertical layers. All simulations were repeated  
 407 using the ocean model configured in isopycnal mode (results were similar and are not pre-  
 408 sented here).

409 Ocean parameters are as specified in the MISOMIP configuration [Asay-Davis et  
 410 al , 2016], and are shown in Table 1. The simulation is initially at rest, with horizontally  
 411 uniform initial ocean temperature and salinity profiles which vary linearly between spec-  
 412 ified surface and bottom values:  $T_{top} = -1.9^\circ$  C,  $T_{bottom} = 1.0^\circ$  C,  $S_{top} = 33.8$  psu,  
 413  $S_{bottom} = 34.7$  psu. The maximum ocean depth is  $H_{ocean} = 720$  m. A sponge layer  
 414 is used on the northern boundary of the domain, which relaxes the temperature and salin-  
 415 ity back to the initial temperature and salinity profile. The sponge layer is  $L_{sponge}=10$   
 416 km long, and has a relaxation time scale parameter  $T_{sponge} = 0.1$  days at the northern  
 417 boundary. The inverse of the relaxation time scale parameter drops linearly to zero over  
 418 the length  $L_{sponge}$ . Melting is set to zero for ocean cells where the ocean column thick-  
 419 ness is less than 10m to avoid using more energy to melt ice than is present in the water  
 420 column.

### 421 3.4 Spinup period:

422 The model is spun-up for 5 years with all ice elements being fixed. During spinup,  
 423 the injection of buoyant meltwater at the base of the ice shelf drives a clockwise circu-  
 424 lation within the domain (not shown). The circulation compares well with an identical  
 425 static ice-shelf experiment run using an Eulerian ice shelf model [Goldberg et al , 2012].  
 426 A detailed comparison of the Lagrangian and Eulerian ice shelf models is presented in a  
 427 separate study, and is not shown here.

### 428 3.5 Iceberg calving:

429 After spinup, a large tabular iceberg detaches from the ice shelf, and allowed to  
 430 drift into the open ocean. This is achieved by allowing all ice elements initially within

431 a 14.4 km radius of the center of the ice front to move freely while the other ice ele-  
 432 ments remain stationary. Ice elements less than 12 km from the center of the ice front,  
 433 are bonded together to form a semi-circular tabular iceberg. A ring of elements whose dis-  
 434 tance,  $d$ , from the ice front center obeys  $12 \text{ km} \leq d \leq 14.4 \text{ km}$ , are allowed to move  
 435 freely, but have all their bonds removed. Elements in this half annulus represent fragments  
 436 of the ice shelf which calve into small pieces during a large calving event.

437 After the spinup period, a wind stress  $\vec{\tau} = <\tau_x, \tau_y> = <0.05, 0.05> \frac{N}{m^2}$  is applied to  
 438 drive the tabular iceberg away from the ice-shelf cavity. This is referred to as the control  
 439 simulation. Perturbation experiments were also performed using other wind stress values.  
 440 Further perturbation experiments were performed by breaking some numerical bonds in  
 441 order to break the tabular iceberg into smaller pieces.

## 4 Model Results

442 After spinup, the elements near the ice-shelf front are allowed to move freely, and  
 443 the icebergs begin to drift away from the ice shelf while fully submerged in the ocean  
 444 (see figures 2 and 7, and the animations in the supplementary materials). At this point,  
 445 the LBIM and the ocean model are fully coupled: changes to the iceberg position alter  
 446 the top-of-ocean pressure and dynamical boundary condition; and changes to the iceberg  
 447 melt rates alter the top-of-ocean temperature, salt and mass fluxes. These changing ocean  
 448 boundary conditions influence the ocean by triggering gravity waves, driving surface mix-  
 449 ing, and affecting the ocean stratification. The evolving ocean velocities, temperatures  
 450 and salinities feedback onto the ice elements by changing the force balance on the ice  
 451 elements (leading to changes in the elements' position), and altering the melt rates. The  
 452 various feedbacks within this coupled system offer many opportunities for the model to  
 453 become unstable. The fact that the model is stable and that we are able to simulate tabu-  
 454 lar icebergs moving in the ocean without the modeling crashing and introducing artificial  
 455 effects like tsunamis, is a non-trivial technical milestone.

### 4.1 Iceberg motion

456 In the control simulation, the semi-circular tabular iceberg moves as a cohesive unit  
 457 due to the presence of the numerical bonds, while the smaller ice fragments quickly dis-  
 458 perse (Figure 2). The tabular iceberg drifts towards the north east, driven by the wind and  
 459 steered by the Coriolis force. As the tabular iceberg drifts northwards, it rotates in a coun-  
 460 terclockwise direction (the direction of the Coriolis force in the Southern Hemisphere),  
 461 and makes contact with the eastern boundary of the domain, before continuing northward.  
 462 Most of the smaller ice fragments also move to the northeast, but not as a cohesive unit.  
 463 Some of these element also move rapidly to other parts of the domain.

464 The direction (and speed) of the iceberg drift is largely determined by the wind  
 465 speed and direction. Perturbation experiments using different wind stresses show that for  
 466 sufficiently large winds, the tabular iceberg drifts to the north east when  $\tau_x > 0$ , and to the  
 467 north west when  $\tau_x < 0$  (not shown). For a purely zonal wind stress with  $|\tau_x| \leq 0.01 \frac{N}{m^2}$ ,  
 468 the iceberg does not move away from the ice shelf. When the wind is purely offshore  
 469 ( $\tau_x = 0.0 \frac{N}{m^2}$ ), a meridional wind stress  $\tau_y \geq 0.05 \frac{N}{m^2}$  is needed to move the tabular ice-  
 470 berg away from the ice shelf. While this result is partly an artifact of the chosen shape  
 471 of the calving iceberg, it is also consistent with Bassis and Jacobs [2013] who noted that  
 472 calving is a two step process consisting of (i) ice-shelf rifting that forms an iceberg and  
 473 (ii) iceberg detachment. The results here suggest that strong (cross-shore) winds may be  
 474 required to drive large tabular icebergs away from their source ice shelves.

477 **4.2 Breaking bonds**

478 The numerical bonds in the LBIM enable the tabular iceberg to retain its shape.  
 479 This is demonstrated by comparing the control simulation to an identical simulation where  
 480 all numerical bonds have been removed (Figure 10). In the bond-free simulation, the ice  
 481 elements quickly move apart from one another (Figure 10b). This bond-free simulation  
 482 does not adequately represent tabular iceberg, which can move long distances through the  
 483 ocean as a cohesive unit. This result motivates the inclusion of numerical in the LBIM  
 484 model, even though they are computationally expensive.

485 By breaking some (but not all) numerical bonds, we can simulate breaking of tab-  
 486 ular icebergs into smaller pieces. Figure ??? shows the results of an experiment which is  
 487 identical to the control experiment, except that all numerical bonds that intersect the line  
 488  $x = \frac{L_x}{2}$  have been severed. This effectively cuts the large tabular iceberg into two halves.  
 489 As the icebergs drift northwards, the two halves of the tabular iceberg each move as a co-  
 490 hesive unit, but they are able to move independently of one other (Figure ???). The two  
 491 large fragments initially move together, but begin to separate after a few days. The break-  
 492 ing of a tabular iceberg has the additional effect of increasing the total surface area of ice  
 493 exposed to the ocean, thus increasing the total decay rate of the icebergs.

494 **4.3 Ocean response**

495 Since the tabular iceberg is submerged in the ocean, the iceberg calving and drift  
 496 affects the the surrounding ocean. In the control simulation, as the tabular iceberg drifts  
 497 northward a warming of the surface waters is observed around the tabular iceberg, with  
 498 the largest warming occurring at the ice-shelf front and along the tabular iceberg's rounded  
 499 edge (Figure 3). This surface warming is caused by upwelling of the warmer waters from  
 500 beneath the ice shelf and iceberg. As the icebergs drifts away from the ice shelf, these  
 501 warmer waters remain at the surface, mapping of the iceberg wake (Figure 3). The motion  
 502 of the tabular iceberg disturbs the ocean surface, which affects ocean velocities through  
 503 out the water column (Figure 8). The elevated shears around the tabular iceberg lead to  
 504 increased vertical mixing in the vicinity of the iceberg, which alters the stratification of  
 505 the water column (Figure 7), heating the upper ocean. The signature of upwelling wa-  
 506 ter in the wake of a drifting tabular iceberg bears some similarity to satellite observations  
 507 of streaks of increased ocean color in the wake of tabular iceberg in the Southern Ocean  
 508 [Duprat et al , 2016], suggesting that the increased productivity around icebergs may be  
 509 driven by upwelling water delivering nutrients to the surface.

510 **4.4 Iceberg melt rates**

511 The increased subsurface velocities and temperatures cause elevated melt rates at  
 512 the base of the ice shelf and iceberg (Figure 9). The largest melt rates are observed at the  
 513 newly calved ice-shelf front and on the rounded side of the tabular iceberg (Figure 9a),  
 514 where the iceberg calving has created steep ice cliffs. These sharp ice fronts allow for  
 515 large ocean currents (Figure 9c), which drive the elevated melt rates. The elevated melt  
 516 rates act to smooth out the ice front over time, making the ice cliff less steep. While this  
 517 is likely a real phenomena that could be observed in nature, we should be wary of the  
 518 modeled velocities at the ice cliffs, since large changes in ice thicknesses are often associ-  
 519 ated with numerical pressure gradient errors which can drive spurious motion.

520 The large melt rates along the ice edges are also partly driven by the fact that dif-  
 521 ferent melt parametrization are used in the interior and edges of large ice structures (see  
 522 Section 2.5). Figure 11 shows the melt rates computed with (a) the 3-equation-model  
 523 parametrization [Holland and Jenkins , 1999], (b) point-particle-iceberg-melt parametriza-  
 524 tion [Gladstone et al , 2001], and (c) the mixed-melt-rate parametrization (from Section  
 525 2.5). The 3-equation-model melt rates (Figure 11a) are about half of those calculated us-

526 ing the point-particle-iceberg-melt parametrization (Figure 11b). When the mixed-melt-rate  
 527 parametrization is used (Figure 11c), the very high melt rates are only observed at the  
 528 edges of ice structures. However, somewhat elevated melt rates at the steep ice cliffs are  
 529 still seen in the simulation using the 3-equation-model parametrization (Figure 11a), in-  
 530 dicating these are not solely caused by our choice of parameterizations, but rather there  
 531 is an underlying dynamical mechanism causing elevated melt rates close to the steep ice  
 532 fronts.

## 533 5 Summary

534 In this study we present a novel framework for simulating tabular icebergs in ocean  
 535 models. In this framework, large tabular icebergs are represented by a collections of La-  
 536 grangian elements that are held together by numerical bonds. Such a representation al-  
 537 lows the icebergs to interact with the ocean across a wide area (larger than a grid cell),  
 538 and behave as if they had a finite size and structure. This is in contrast to previous rep-  
 539 resentations of icebergs in numerical models [Jongma et al , 2009; Martin and Adcroft ,  
 540 2010; Marsh et al , 2015] that treat icebergs as point particles. Explicitly resolving tabu-  
 541 lar icebergs in the ocean allows the icebergs to interact with the ocean in a more realistic  
 542 way, and allows us to study the effects that tabular icebergs have on the ocean circulation.  
 543 Including numerical bonds between elements allows for simulation iceberg calving and  
 544 fracture by breaking the bonds.

545 The capabilities of the tabular iceberg model were demonstrated by modeling a tabu-  
 546 lar iceberg drifting away from an idealized ice shelf (also constructed using Lagrangian  
 547 elements). The results show that explicitly resolving the iceberg in the ocean allowed for a  
 548 complex interaction between the tabular iceberg and the surrounding ocean. In our setup,  
 549 the tabular iceberg is driven away from the ice shelf by ocean currents, wind stress, and  
 550 the Coriolis force. As the iceberg moves through the water, it disturbs the ocean surface,  
 551 driving ocean currents. The motion of the iceberg and melt beneath the iceberg drive up-  
 552 welling along the sides of the iceberg, which entrains ambient water and causes a warm-  
 553 ing of the surface ocean in the wake of the iceberg. The changing ocean conditions feed  
 554 back onto the iceberg, affecting its motion and melt rates. The highest melt rates are ob-  
 555 served at edge of the iceberg which has the steepest ice cliff. These have the effect of  
 556 smoothing out the ice edge over time. Simulations without using numerical bonds showed  
 557 that these bonds are essential for allowing the iceberg to move as a unit. We also demon-  
 558 strate that by breaking these numerical bonds we can simulate iceberg fracture, which is  
 559 important process that increases the rate of iceberg decay.

560 To our knowledge, the model presented in this study is the first model to explicitly  
 561 resolve drifting tabular icebergs in an ocean model that can be used for climate studies. A  
 562 natural extension of this work is a representation of tabular icebergs in a general circula-  
 563 tion model (GCM). However, before this can be done, there are a number of issues that  
 564 need to be resolved: firstly, the question of how and when to introduce tabular icebergs  
 565 into the ocean needs to be addressed. For GCM's with active ice shelves, a calving law is  
 566 needed to release the tabular iceberg into the ocean. The question of what calving law to  
 567 use is a topic of ongoing research [Benn et all , 2007; Alley et al , 2008; Levermann et al  
 568 , 2012; Bassis and Jacobs , 2013] and is still unresolved. One potential way to temporarily  
 569 bypass this problem would be to run hindcast simulations using historically observed calv-  
 570 ing events. A related issue is the question of how and when to break the bonds within the  
 571 freely floating icebergs to simulation iceberg breakup. Without a rule for iceberg breakup,  
 572 the tabular icebergs would likely drift to unrealistically low latitudes. Another challenge  
 573 will be to develop methods to initialize the size and positions of elements on a spherical  
 574 grid. This study used a cartesian coordinate system, which allowed us to initialize the ice  
 575 elements in a regular staggered lattice. A different initialization method will be needed to  
 576 generalize this initialization procedure to curved coordinates which are needed for large-  
 577 scale global simulations. Further work is also needed to understand (and model) the in-

teractions between tabular icebergs and sea ice, and to parametrize the effects of iceberg grounding, as these interactions play a large role in dictating the trajectories of tabular icebergs. However, despite these remaining challenges, the technical framework described in this article is potentially a using step towards including tabular icebergs in global GCM's, and hence a step towards making more accurate projections of future sea level.

## 6 Appendix A

### 6.1 Environmental forces on ice elements

The non-interactive forces on an ice element are as described in [Martin and Adcroft , 2010], and are repeated here for completeness. The forces on an element due to air (a), ocean (o) and sea ice (si) drag are given by

$$(\vec{F}_a) = \rho_a (0.5c_{a,v}WF + c_{a,h}LW)|\vec{u}_a - \vec{u}|(\vec{u}_a - \vec{u}), \quad (11)$$

$$(\vec{F}_o) = \rho_o (0.5c_{o,v}W(D - T_{si})F + c_{o,h}LW)|\vec{u}_o - \vec{u}|(\vec{u}_o - \vec{u}), \quad (12)$$

$$(\vec{F}_{si}) = \rho_{si} (0.5c_{si,v}WT_{si}F + c_{si,h}LW)|\vec{u}_{si} - \vec{u}|(\vec{u}_{si} - \vec{u}). \quad (13)$$

Here  $\rho_a$ ,  $\rho_o$ ,  $\rho_{si}$ , are the density of air, ocean and sea ice, respectively.  $c_{a,v}$ ,  $c_{o,v}$  and  $c_{si,v}$  are the vertical drag coefficients with air, ocean and sea ice, while  $c_{a,h}$ ,  $c_{o,h}$  and  $c_{si,h}$  are the respective horizontal drag coefficients.  $\vec{u}_a$ ,  $\vec{u}_o$ ,  $\vec{u}_{si}$ , are the velocities air, ocean and sea ice, respectively. L, W, T, F and D are the length, width, thickness, free-board and draft of the ice element. The element thickness is related to the draft and free-board by  $T = F + D$  and  $D = \frac{\rho}{\rho_o}T$ , where  $\rho$  is the ice element density.  $T_{si}$  is the sea ice thickness.

The wave radiation force ( $\vec{F}_R$ ) is given by

$$\vec{F}_R = \frac{1}{2}\rho_o c_{wd} g a \min(a, F) 2 \frac{WL}{W+L} \frac{\vec{v}_a}{|\vec{v}_a|} \quad (14)$$

where g is the acceleration due to gravity, a is the wave amplitude empirically related to the wind speed by  $a = 0.010125|\vec{v}_a - \vec{v}_o|$ , and  $c_{wd}$  is the wave drag coefficient defined as

$$c_{wd} = 0.06 \min\left( \max\left[ 0, \frac{L - L_c}{L_t - L_c} \right], 1 \right), \quad (15)$$

where  $L_w = 0.32|\vec{v}_a - \vec{v}_o|^2$  is an empirical wave length,  $L_c = 0.125L_w$  is the cutoff length, and  $L_t = 0.25L_w$  is the upper limit.

The pressure gradient force is approximated as a force due to sea surface slope and given by

$$\vec{F}_{SS} = -Mg\vec{\nabla}\eta \quad (16)$$

where  $\eta$  is the sea surface height.

### 6.2 Melt rate parametrization

As discussed in Section 2.5, unbounded ice elements in the LBIM decay according to parameterizations for iceberg decay typically used in iceberg drift models [Martin and Adcroft , 2010], while ice elements within larger ice structures have only a basal melt given by the three equation model [Holland and Jenkins , 1999] .

For unbonded ice elements, the element thickness decays due to basal melt at a rate  $M_b$ , while the length and width of the elements decay as a result of melt due to wave erosion,  $M_e$ , and melt due to buoyant convection,  $M_v$ . Following Gladstone et al [2001] and

Martin and Adcroft [2010], the basal melt rate, wave erosion melt rate, and buoyant convection melt rate are parameterized by

$$M_b = 0.58|\vec{v} - \vec{v}_0|^{0.8} \frac{\tilde{T}_0 - \tilde{T}}{L^{0.2}} \quad (17)$$

$$M_e = \frac{1}{12} S_s \left( 1 + \cos [\pi A_i^3] \right) \left( \tilde{T}_0 + 2 \right), \quad (18)$$

$$M_v = \left( 7.62 \times 10^{-3} \right) \tilde{T}_0 + \left( 1.29 \times 10^{-3} \right) \tilde{T}_0^2. \quad (19)$$

$\tilde{T}$  is the effective iceberg temperature and is set to  $\tilde{T} = 4^\circ\text{C}$ ,  $\tilde{T}_0$  is the temperature at the top of the ocean,  $A_i$  is the sea ice area fraction, and  $S_s$  is the sea state, which is given by the Beaufort scale

$$S_s = \frac{2}{3} |\vec{u}_a - \vec{u}_o|^{\frac{1}{2}} + \frac{1}{10} |\vec{u}_a - \vec{u}_o| \quad (20)$$

All three melt rates are in units of meters per day.

For elements inside larger structures, the melt due to wave erosion and melt due to buoyant convection are set to zero, and the basal melt,  $M_s$  is given by the standard three equation model [Holland and Jenkins , 1999].

## 7 Appendix B

### 7.1 Modified Verlet Algorithm

The LBIM uses a version velocity Verlet time-stepping algorithm, which has been modified to allow part of the forcing to be calculated implicitly. The traditional velocity Verlet algorithm is commonly used in molecular dynamics, as it is simple to implement, second order accurate and computationally efficient [Swope et al , 1982; Omelyan et al , 2002]. Here we modify the traditional scheme to allow for the drag forces to be modeled implicitly, which prevents large accelerations for element's whose mass approaches zero. To do this, we include both an implicit and explicit acceleration,  $a = a^{exp} + a^{imp}$ . The explicit acceleration,  $a^{exp}$  includes all forcing terms which depend only on the previous time step and the current position, while the implicit acceleration,  $a^{imp}$  includes forcing terms which depend on the velocity at the current time step (in particular the drag and Coriolis forces).

Using a time step of  $\Delta t$ , and subscripts to denote the time step (so that  $t_{n+1} = t_n + \Delta t$ ), the modified velocity Verlet scheme can be written as:

$$1) x_{n+1} = x_n + u_n \Delta t + \frac{1}{2} \Delta t^2 \left( a_n^{exp} + a_n^{imp} \right).$$

$$2) \text{Calculate } a_{n+1}^{exp}$$

$$3) \text{Calculate } a_{n+1}^{imp} \text{ and } u_{n+1} = u_n + \frac{\Delta t}{2} \left( a_n^{exp} + a_{n+1}^{exp} \right) + (\Delta t) a_{n+1}^{imp}$$

This scheme reduces to the traditional velocity Verlet when  $a^{imp}$  is set to zero.

Note that  $a_{n+1}^{exp} = a_{n+1}^{exp}(x_{n+1}, t_n)$  is an explicit function of  $x_{n+1}$  and other quantities evaluated at time  $t_n$ , while  $a_{n+1}^{imp} = a_{n+1}^{imp}(u_{n+1}, x_{n+1}, t_n)$  additionally depends on  $u_{n+1}$ , and needs to be solved implicitly. For this reason in step three,  $a_{n+1}^{imp}$  and  $u_{n+1}$  need to be solved simultaneously, as described in the next subsection.

In equation (1), the forces due to ocean drag, atmospheric drag and sea ice drag are treated implicitly. The force due to sea surface slope and wave radiation are treated explicitly. The Coriolis term is handled using Crank-Nicolson scheme so that half of the effect is implicit and half is explicit. The elastic part of the interactive forces is treated explicitly, while the interactive damping is handled semi-implicitly in that the drag force on element A by element B depends on the velocities of elements A and B evaluated at time  $t_{n+1}$  and  $t_n$ , respectively.

## 654 7.2 Solving for the velocity implicitly

655 Since this modified scheme contains some forcing terms which are handled implicitly,  
 656  $a_{n+1}^{imp}$  and  $u_{n+1}$  need to be calculated simultaneously. We demonstrate how this is  
 657 done, using a simplified one-dimensional version of equation (1), neglecting the atmo-  
 658 spheric drag, sea ice drag and Coriolis force, so that the only implicitly treated term is the  
 659 ocean drag. In this demonstration, we use a superscript to denote the ocean drag force,  
 660  $F^o$ , and ocean velocity,  $u^o$ , to avoid confusion with the subscripts indicating time step.  
 661 We also define an explicit force,  $F^{exp}$ , which accounts for all forces not proportional the  
 662 element velocity. With these simplifications, the implicit and explicit accelerations are

$$663 \quad a^{exp} = \frac{1}{M}(\vec{F}^{exp}) \quad (21)$$

$$663 \quad a^{imp} = \frac{1}{M}(F^o) \quad (22)$$

664 The ocean drag force at time  $t_{n+1}$  is modeled (mostly) implicitly as

$$665 \quad F_{n+1}^o = \tilde{c}^o |u_n^o - u_n| (u_n^o - u_{n+1}), \quad (23)$$

665 where  $\tilde{c}^o$  is the effective drag coefficient, accounting for the dimensions of the ice element  
 666 (see equation 12).

667 Step 3 of the modified velocity Verlet scheme can be rewritten by introducing an  
 668 intermediate velocity  $u^*$ , which only depends on the velocity and acceleration at time  $t_n$ ,

$$669 \quad u_n^* = u_n + \frac{1}{2}(\Delta t)a_n^{exp}. \quad (24)$$

Using this, the updated velocity (Step 3) can be written

$$666 \quad u_{n+1} = u_n^* + \frac{\Delta t}{2}a_{n+1}^{exp} + (\Delta t)a_{n+1}^{imp}. \quad (25)$$

670 Including the forcing terms into this equations gives

$$671 \quad u_{n+1} = u_n^* + \frac{\Delta t}{2M}(F_{n+1}^{exp}) + \frac{\Delta t}{M} \left( c_w |u_n^o - u_n| (u_n^o - u_{n+1}) \right) \quad (26)$$

Solving for  $u(t_{n+1})$  in terms of quantities which only depend on the previous time step  
 gives

$$672 \quad u_{n+1} = \frac{u_n^* + \frac{\Delta t}{2M}(F_{n+1}^{exp}) + \frac{\Delta t}{M} \left( c_w |u_n^o - u_n| (u_n^o) \right)}{\left( 1 + \frac{\Delta t}{M} c_w |u_n^o - u_n| \right)} \quad (27)$$

Once the  $u_{n+1}$  has been found, it can be used to calculate the explicit and implicit accelerations, which are required for the next time step.

Finally, we note that the the drag term (equation 23) is not entirely implicit, since the element velocity inside the absolute value is evaluated at time  $t_n$ , rather than at time  $t_{n+1}$ . This is done so that we can solve for the updated velocity analytically. One consequence of this is that it can give rise to a small oscillation in the element velocity. This oscillation is addressed by using a predictive corrective scheme: after solving for a first guess of the velocity at time  $t_{n+1}$ , this estimate of the velocity is used to update the estimate of the drag force (i.e.: inside the absolute value signs). This updated drag, can now be used to repeat the process described above to find an improved estimate of the velocity. We found that two iterations were sufficient to remove the unwanted oscillation.

The procedure described in this section is easily extended to include more forcing terms and two dimensions (where it involves inverting a  $2 \times 2$  matrix).

## 686 8 Appendix C

### 687 **Connecting bonds across processor boundaries**

688 Since the LBIM is parallelized across multiple processors, it often happens that two  
 689 elements on different processes are bonded together. Keeping track of numerical bonds  
 690 across processor boundaries requires a lot of book keeping. In this section we describe the  
 691 how LBIM handles bonds across processor boundaries.

692 The basics of the bond bookkeeping work as follows: consider an element A and  
 693 an element B that are bonded together. Each element has a copy of the bond (a piece of  
 694 memory which describes the bond between the two elements), which is stored with the  
 695 element. Let A-B be the bond stored by element A, and B-A be the bond stored by ele-  
 696 ment B. Bond A-B contains a pointer which points to element B and bond B-A contains a  
 697 pointer which points to element A.

698 Consider a situation where element A and B are originally on Processor 1, and then  
 699 element B moves to Processor 2. When this occurs, the memory assigned to element B  
 700 on processor 1 is removed, and is allocated on Processor 2. This means that the pointer  
 701 to element B in bond A-B (stored in element A on Processor 1) is no longer assigned.  
 702 Similarly, the pointer to element A in bond B-A (stored in element B on Processor 2) is  
 703 no longer assigned. Before the next time step, a halo update occurs, so that the there is  
 704 a copy of element A in the halo of Processor 2 and a copy of element B in the halo of  
 705 Processor 1. After the halo update, the bonds A-B and B-A have to be reconnected on  
 706 both Processor 1 and 2. To aid in reconnecting the bonds, a copy of the grid cell number  
 707 of element B is stored in the bond A-B and a copy of the grid cell number of element A  
 708 is stored in the bond B-A. We refer to this as the ‘most recent address’. Before a bond  
 709 is moved from one processor to another, the ‘most recent address’ is updated, so that the  
 710 bond can be reconnected later. To reconnect bond A-B on Processor 1 (for example), we  
 711 find the most recent address of element B, and search through the list of elements in the  
 712 grid cell corresponding to the most recent address of element B until element B is found.  
 713 The pointer to element B in bond A-B is reassigned, and the bond is said to be connected.

714 The reconnected bond A-B (stored in element A) is said to be working properly  
 715 when the following four test pass:

- 716 1. The pointer to element B is assigned on bond A-B.
- 717 2. The corresponding bond B-A exists on element B.
- 718 3. A pointer to element A exists in this bond B-A.
- 719 4. The element A which is being pointed to is the same element A where you started.

720 A useful tool disconnecting and reconnecting bonds is that each element is assigned a  
 721 unique number so that elements are easily identified.

722      **Acknowledgments**

723      = enter acknowledgments here =

## 724 References

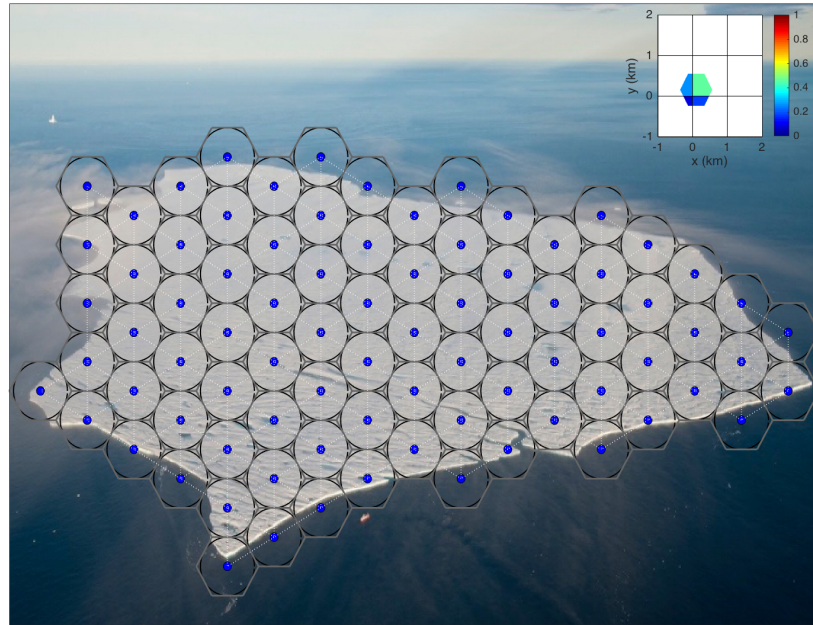
- 725 Asay-Davis, X. S., S. L. Cornford, B. K. Galton-Fenzi, R. M. Gladstone, G. H. Gud-  
 726 mundsson, D. M. Holland, P. R. Holland, and D. F. Martin (2016), Experimental de-  
 727 sign for three interrelated marine ice sheet and ocean model intercomparison projects:  
 728 MISMIP v. 3 (MISMIP+), ISOMIP v. 2 (ISOMIP+) and MISOMIP v. 1 (MISOMIP1).  
 729 *Geoscientific Model Development* 9, no. 7: 2471.
- 730 Arrigo, K. R., G. L. van Dijken, D. G. Ainley, M. A. Fahnestock, and T. Markus (2002).  
 731 Ecological impact of a large Antarctic iceberg. *Geophys. Res. Lett.*, 29(7).
- 732 Alley, R. B., H. J. Horgan, I. Joughin, K. M. Cuffey, T. K. Dupont, B. R. Parizek, S.  
 733 Anandakrishnan, and J. Bassis (2008), A simple law for ice-shelf calving. *Science* 322,  
 734 no. 5906, 1344-1344.
- 735 Bassis, J. N., and S. Jacobs (2013), Diverse calving patterns linked to glacier geometry.  
 736 *Nature Geoscience*, 6(10), 833-836.
- 737 Benn, D. I., C. R. Warren, and R. H. Mottram (2007). Calving processes and the dynam-  
 738 ics of calving glaciers. *Earth-Science Reviews*, 82(3), 143-179.
- 739 Bigg, G. R., Wadley, M. R., Stevens, D. P., and Johnson, J. A. (1997), Modeling the dy-  
 740 namics and thermodynamics of icebergs. *Cold Regions Science and Technology*, 26(2),  
 741 113-135.
- 742 Borstad, C. P., A. Khazendar, E. Larour, M. Morlighem, E. Rignot, M. P. Schodlok, and  
 743 H. Seroussi (2012), A damage mechanics assessment of the Larsen B ice shelf prior to  
 744 collapse: Toward a physically-based calving law, *Geophys. Res. Lett.*, 39, L18502
- 745 Biddle, L. C., J. Kaiser, K. J. Heywood, A. F. Thompson and A. Jenkins (2015), Ocean  
 746 glider observations of iceberg-enhanced biological productivity in the northwestern  
 747 Weddell Sea, *Geophys. Res. Lett.*, 42, 459-465.
- 748 De Rydt, J., and G. H. Gudmundsson (2016), Coupled ice shelf ocean modeling and com-  
 749 plex grounding line retreat from a seabed ridge. *J. of Geophys. Res.: Earth Surface*,  
 750 121(5), 865-880.
- 751 Dunne, J.P., J.G. John,, A.J. Adcroft, S.M. Griffies, R.W. Hallberg, E. Shevliakova, R.J.  
 752 Stouffer, W. Cooke, K.A. Dunne, M.J Harrison, and J.P. Krasting (2012), GFDL's  
 753 ESM2 global coupled climate-carbon Earth System Models. Part I: Physical formula-  
 754 tion and baseline simulation characteristics. *J. of Climate*, 25(19), 6646-6665.
- 755 Depoorter, M. A., J. L. Bamber, J. A. Griggs, J. T. M. Lenaerts, Stefan RM Ligtenberg,  
 756 M. R. van den Broek, and G. Moholdt (2013), Calving fluxes and basal melt rates of  
 757 Antarctic ice shelves. *Nature*, 502(7469), 89-92.
- 758 Determan J., Gerdes R. (1994), Melting and freezing beneath ice shelves: implications  
 759 from a three-dimensional ocean-circulation model. *Ann. Glaciol.*, 20, 413-419.
- 760 Dowdeswell, J. A., and J. L. Bamber (2007), Keel depths of modern Antarctic icebergs  
 761 and implications for sea-floor scouring in the geological record. *Marine Geology*,  
 762 243(1), 120-131.
- 763 Duprat, L. P., G. R. Bigg, and D. J. Wilton (2016), Enhanced Southern Ocean marine pro-  
 764 ductivity due to fertilization by giant icebergs. *Nature Geoscience*.
- 765 Eckert, E. R. G. (1950). Introduction to the Transfer of Heat and Mass. McGraw-Hill.
- 766 Fogwill, C.J., E. van Sebille, E.A. Cougnon, C.S. Turney, S.R. Rintoul, B.K. Galton-Fenzi,  
 767 G.F. Clark, E.M. Marzinelli, E.B. Rainsley, and L. Carter (2016), Brief communication:  
 768 Impacts of a developing polynya off Commonwealth Bay, East Antarctica, triggered by  
 769 grounding of iceberg B09B. *The Cryosphere*, 10(6), p.2603.
- 770 Gladstone, R. M., G. R. Bigg, and K. W. Nicholls. (2001), Iceberg trajectory model-  
 771 ing and meltwater injection in the Southern Ocean (1978-2012). *J. of Geophys. Res.:*  
 772 *Oceans*, 106(C9), 19903-19915.
- 773 Goldberg, D. N., C. M. Little, O. V. Sergienko, A. Gnanadesikan, R. Hallberg, and M.  
 774 Oppenheimer (2012), Investigation of land ice/ocean interaction with a fully coupled  
 775 ice-ocean model: 1. Model description and behavior. *J. of Geophys. Res.: Earth Surface*,  
 776 117(F2).

- 777 Gladish, C. V., D. M. Holland, P. R. Holland, and S. F. Price (2012), Ice-shelf basal chan-  
 778 nels in a coupled ice/ocean model. *J. of Glaciol.*, 58(212), 1227-1244.
- 779 Grosfeld K., R. Gerdes, J. Determan (1997), Thermohaline circulation and interaction  
 780 between ice shelf cavities and the adjacent open ocean. *J. Phys. Oceanogr.*, **102**, C7,  
 781 15959-15610.
- 782 Grosfeld, K., and H. SandhŁger, (2004). The evolution of a coupled ice shelfDocean sys-  
 783 tem under different climate states. *Global and Planetary Change*, 42(1), 107-132.
- 784 Hallberg, R., A. Adcroft, J. P. Dunne, J. P., Krasting, R. J., and Stouffer (2013), Sensitiv-  
 785 ity of twenty-first-century global-mean steric sea level rise to ocean model formulation.  
 786 *J. of Climate*, 26(9), 2947-2956.
- 787 Holland D. M., Jenkins A. (2001), Adaptation of an isopycnic coordinate ocean model for  
 788 the study of circulation beneath ice shelves. *Mon. Wea. Rev.*, 129, 1905-1927.
- 789 Holland P. R. and D. L. Feltham (2006), The effects of rotation and ice shelf topography  
 790 on frazil-laden Ice Shelf Water plumes. *J. Phys. Oceanogr.*, 36, 2312-2327.
- 791 Holland, D. M., and A. Jenkins (1999), Modeling thermodynamic ice-ocean interactions at  
 792 the base of an ice shelf. *J. of Phys. Oceanogr.* 29.8, 1787-1800.
- 793 Hellmer H.H., Olbers D. J. (1989), A two-dimensional model for the thermohaline circula-  
 794 tion under an ice shelf. *Antarctic Science*, 1, 325- 336.
- 795 Henderson J., J. S. P. Loe (2016), The Prospects andChallenges for Arctic Oil Develop-  
 796 ment. *Oil, Gas and Energy Law Journal (OGEL)*, 14 (2)
- 797 Hopkins, M. A. (1996). On the mesoscale interaction of lead ice and floes. *J. of Geophys.*  
 798 *Res.: Oceans*, 101(C8), 18315-18326.
- 799 Hopkins, M. A. (2004). A discrete element Lagrangian sea ice model. *Engineering Com-  
 800 putations*, 21(2/3/4), 409-421.
- 801 Gaskill, H. S., and J. Rochester (1984). A new technique for iceberg drift prediction. *Cold*  
 802 *Reg. Sci. Technol.*, 8(3), 223-234.
- 803 Jacobs, S. S., H. H. Helmer, C. S. M. Doake, A. Jenkins, R. M. Frolich (1992), Melting  
 804 of ice shelves and the mass balance of Antarctica. *J. of Glaciol.*, 38(130), 375-387.
- 805 Jakobsen, T. (2001). Advanced character physics. In *Game Developers Conference*, Vol. 3.
- 806 Jenkins, A., P. Dutrieux, S. S. Jacobs, S. D. McPhail, J. R. Perrett, A. T. Webb, and D.  
 807 White (2010), Observations beneath Pine Island Glacier in West Antarctica and implica-  
 808 tions for its retreat. *it Nature Geo.*, 3(7), 468-472.
- 809 Jacobs, S. S., A. Jenkins, C. F. Giulivi, and P. Dutrieux (2011). Stronger ocean circulation  
 810 and increased melting under Pine Island Glacier ice shelf. *Nature Geo.*, 4(8), 519-523.
- 811 Jongma, J. I., E. Driesschaert, T. Fichefet, H. Goosse, and H. Renssen (2009), The ef-  
 812 fect of dynamic-thermodynamic icebergs on the Southern Ocean climate in a three-  
 813 dimensional model, *Ocean Modell.*, 26, 104D113.
- 814 Kubat I., M. Sayed, S. Savage, T. Carrières (2005), An operational model of iceberg drift  
 815 *Int. J. Off. Polar Eng.*, 15 (2), 125D131
- 816 Lewis E.L. and R.G. Perkin (1986), Ice pumps and their rates. *J. of Geophys. Res.*, 91,  
 817 11756-11762.
- 818 Losch, M. (2008). Modeling ice shelf cavities in a z coordinate ocean general circulation  
 819 model. *J. of Geophys. Res.: Oceans*, 113(C8).
- 820 Li, B., H. Li, Y. Liu, A. Wang and S. Ji (2014), A modified discrete element model for  
 821 sea ice dynamics. *Acta Oceanologica Sinica*, 33(1), 56-63.
- 822 Liu, M. B. and G. R. Liu (2010), Smoothed particle hydrodynamics (SPH): an overview  
 823 and recent developments. *Archives of computational methods in engineering*, 17(1), 25-  
 824 76.
- 825 Lichéy, C., and H. H. Hellmer (2001). Modeling giant-iceberg drift under the influence of  
 826 sea ice in the Weddell Sea, Antarctica. *J. of Glaciol.*, 47(158), 452-460.
- 827 Levermann, A., T. Albrecht, R. Winkelmann, M. A. Martin, M. Haseloff, and I. Joughin.  
 828 (2012), Kinematic first-order calving law implies potential for abrupt ice-shelf retreat.  
 829 *The Cryosphere*, 6(2), 273-286.

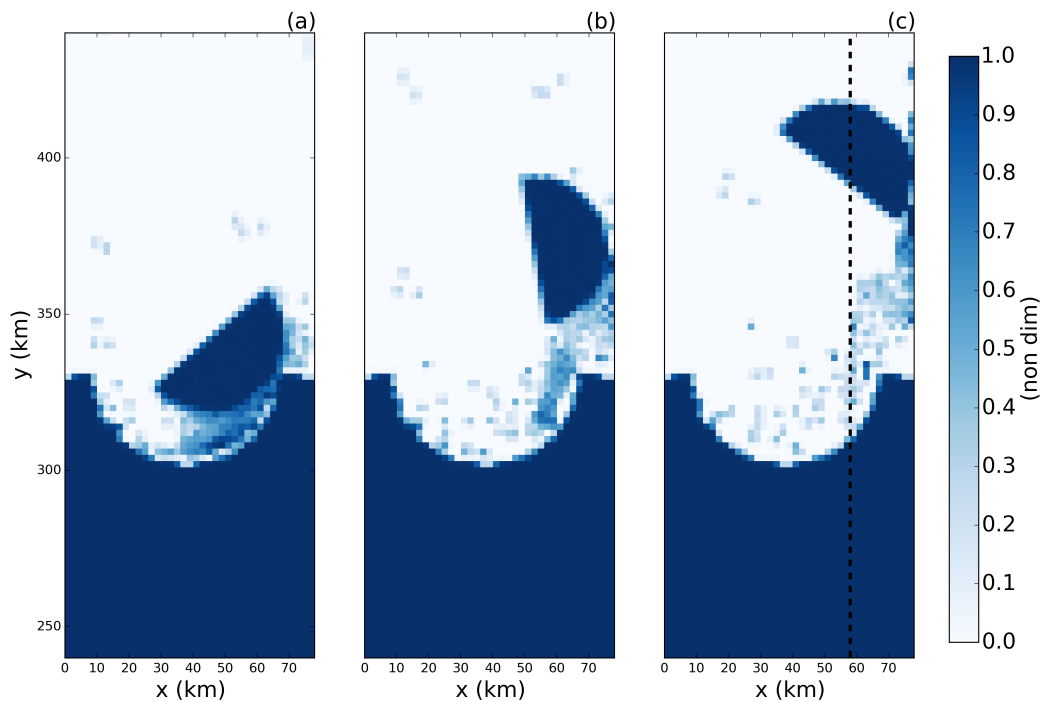
- 830 Mountain, D. G. (1980). On predicting iceberg drift. *Cold Reg. Sci. Technol.*, 1(3-4), 273-  
831 282.
- 832 Martin, T., and Adcroft, A. (2010), Parameterizing the fresh-water flux from land ice to  
833 ocean with interactive icebergs in a coupled climate model. *Ocean Modelling*, 34(3),  
834 111-124.
- 835 Marsh, R., V. O. Ivchenko, N. Skliris, S. Alderson, G. R. Bigg, G. Madec, A. T. Blaker  
836 Y. Aksenov, B. Sinha, A.C. Coward, and J.L. Sommer (2015), NEMODICB (v1. 0):  
837 interactive icebergs in the NEMO ocean model globally configured at eddy-permitting  
838 resolution. *Geoscientific Model Development* 8, no. 5 (2015): 1547-1562.
- 839 MacAyeal D.R. (1984), Thermohaline Circulation Below the Ross Ice Shelf: A Conse-  
840 quence of Tidally Induced Vertical Mixing and Basal Melting. *J. Geophys. Res.*, 89,  
841 597-606
- 842 Merino, N., Le Sommer, J., Durand, G., Jourdain, N. C., Madec, G., Mathiot, P., and  
843 Tournadre, J. (2016), Antarctic icebergs melt over the Southern Ocean: climatology and  
844 impact on sea ice. *Ocean Modelling*, 104, 99-110.
- 845 Nicholls K.W. (1996), Temperature variability beneath Ronne Ice Shelf, Antarctica, from  
846 thermistor cables. *J. Phys. Oceanogr.*, 11, 1199-1210.
- 847 Nicholls KW, Østerhus S, Makinson K (2009), Ice-Ocean processes over the continental  
848 shelf of the southern Weddell Sea, Antarctica: a review. *Rev. Geophys.* 47(3).
- 849 Omelyan, I. P., M. I. Mryglod, and R. Folk (2002), Optimized Verlet-like algorithms for  
850 molecular dynamics simulations. *Physical Review E*, 65(5), 056706.
- 851 Rabatel, M., S. LabbÓ and J. Weiss (2015). Dynamics of an assembly of rigid ice floes. *J.*  
852 *of Geophys. Res.: Oceans*, 120(9), 5887-5909.
- 853 Rignot, E., S. Jacobs, J. Mouginot, and B. Scheuchl (2013), Ice-shelf melting around  
854 Antarctica. *Science*, 341, no. 6143 (2013): 266-270.
- 855 Robinson, N. J., M. J. M. Williams, P. J. Barrett, and A. R. Pyne (2010), Observations of  
856 flow and ice-ocean interaction beneath the McMurdo Ice Shelf, Antarctica, *J. Geophys.*  
857 *Res.*, 115, C03025
- 858 Pizzolato, L., S. E. Howell, C. Derksen, J. Dawson, L. Copland (2014), Changing sea ice  
859 conditions and marine transportation activity in Canadian Arctic waters between 1990  
860 and 2012, *Climatic Change* 123 (2), 161173.
- 861 Pan, W., A. M. Tartakovsky, and J. J. Monaghan (2013). Smoothed particle hydrodynam-  
862 ics non-Newtonian model for ice-sheet and ice-shelf dynamics. *J. of Comp. Phys.*, 242,  
863 828-842.
- 864 Pralong, A., and M. Funk (2005), Dynamic damage model of crevasse opening and appli-  
865 cation to glacier calving, *J. Geophys. Res.*, 110, B01309.
- 866 Sergienko, O. V. (2013). Basal channels on ice shelves. *J. of Geophys. Res.: Earth Surface*,  
867 118(3), 1342-1355.
- 868 Silva, T. A. M., Bigg, G. R., and Nicholls, K. W. (2006), Contribution of giant icebergs to  
869 the Southern Ocean freshwater flux. *J. of Geophys. Res.: Oceans*, 111(C3).
- 870 Smith, K., B. Robison, J. Helly, R. Kaufmann, H. Ruhl, H., T. Shaw, and M. Vernet  
871 (2007), Free-drifting icebergs: Hotspots of chemical and biological enrichment in the  
872 Weddell Sea, *Science*, 317, 478-482.
- 873 Shepherd, A., and D. Wingham (2007). Recent sea-level contributions of the Antarctic and  
874 Greenland ice sheets. *Science*, 315(5818), 1529-1532.
- 875 Stern, A. A., D. M. Holland, P. R. Holland, A. Jenkins and J. Sommeria (2014), The ef-  
876 fect of geometry on ice shelf ocean cavity ventilation: a laboratory experiment. *Experi-  
877 ments in Fluids*, 55(5), 1-19.
- 878 Stern, A.A., Johnson, E., Holland, D.M., Wagner, T.J., Wadhams, P., Bates, R., Abraham-  
879 sen, E.P., Nicholls, K.W., Crawford, A., Gagnon, J. and Tremblay, J.E. (2015), Wind-  
880 driven upwelling around grounded tabular icebergs. *J. of Geophys. Res.: Oceans*, 120(8),  
881 5820-5835.
- 882 Stern, A. A., A. Adcroft, and O. Sergienko (2016), The effects of Antarctic iceberg calv-  
883 ing size distribution in a global climate model. *J. of Geophys. Res.: Oceans*, 121(8),

- 884 5773-5788.
- 885 Swope, W. C., H. C. Andersen, P. H. Berens, and K. R. Wilson (1982), A computer sim-  
886 ulation method for the calculation of equilibrium constants for the formation of physi-  
887 cal clusters of molecules: Application to small water clusters. *The Journal of Chemical*  
888 *Physics* 76, no. 1, 637-649.
- 889 Tournadre, J., N. Bouhier, F. Girard-Ardhuin, and F. RÖmy (2016), Antarctic icebergs dis-  
890 tributions 1992-2014. *J. Geophys Res: Oceans*.
- 891 Turnbull I.D., N. Fournier, M. Stolwijk, T. Fosnaes, D. McGonigal (2015), Operational  
892 iceberg drift forecasting in Northwest Greenland, *Cold Reg. Sci. Technol.* 110, 1-18
- 893 Unger, J. D., 2014. Regulating the Arctic Gold Rush: Recommended Regulatory Reforms  
894 to Protect Alaska's Arctic Environment from Offshore Oil Drilling Pollution . *Alaska L.*  
895 *Rev*, 31
- 896 Vernet, M., et al. (2012), Islands of ice: Influence of free-drifting Antarctic icebergs on  
897 pelagic marine ecosystems, *Oceanography*, 25(3), 38D39
- 898 Wagner, T. J., Wadhams, P., Bates, R., Elosegui, P., Stern, A., Vella, D., E. P. Abraham-  
899 sen, A. Crawford, and Nicholls, K. W. (2014), The ÒfootlooseÓ mechanism: Iceberg  
900 decay from hydrostatic stresses. *Geophys. Res. Lett.*, 41(15), 5522-5529.
- 901 Weeks, W. F., and W. J. Campbell (1973). Icebergs as a fresh-water source: an appraisal.  
902 *J. of Glaciol.*, 12(65), 207-233.
- 903 White, L., A. Adcroft, and R. Hallberg (2009), High-order regridding-remapping schemes  
904 for continuous isopycnal and generalized coordinates in ocean models. *J. of Comp.*  
905 *Phys.*, 228(23), 8665-8692.

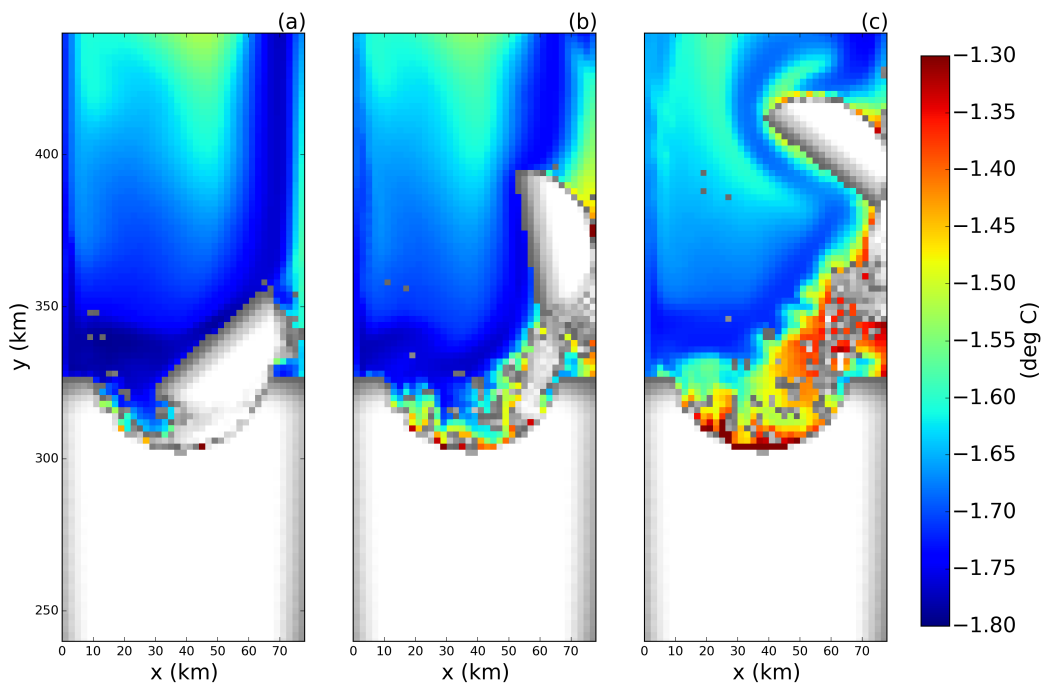
Parameter	Symbol	Value	Unit
Domain Length	$L_x$	80	km
Domain Width	$L_y$	480	km
Horizontal Resolution	$\Delta x$	2	km
Number of vertical layers	$N_l$	72	non-dim
Horizontal Viscosity	$\nu_H$	6.0	$\frac{m^2}{s}$
Diapycnal Viscosity	$\nu_V$	$10^{-3}$	$\frac{m^2}{s}$
Horizontal Diffusivity	$\epsilon_H$	1.0	$\frac{m^2}{s}$
Diapycnal Diffusivity	$\epsilon_V$	$5 \times 10^{-5}$	$\frac{m^2}{s}$
Initial Surface Temperature	$T_t$	-1.9	°C
Initial Bottom Temperature	$T_b$	1.0	°C
Initial Surface Salinity	$S_t$	33.8	psu
Initial Bottom Salinity	$S_b$	34.7	psu
Maximum Ocean depth	$H_{ocean}$	720	m
Relaxation Time of Sponge Layer	$T_{sponge}$	0.1	days
Length of Sponge Layer	$L_{sponge}$	10	km
Time Step for Static Shelf Experiment	$dt_{Static}$	1000	s
Time Step for Iceberg Calving Experiment	$dt_{Calving}$	10	s



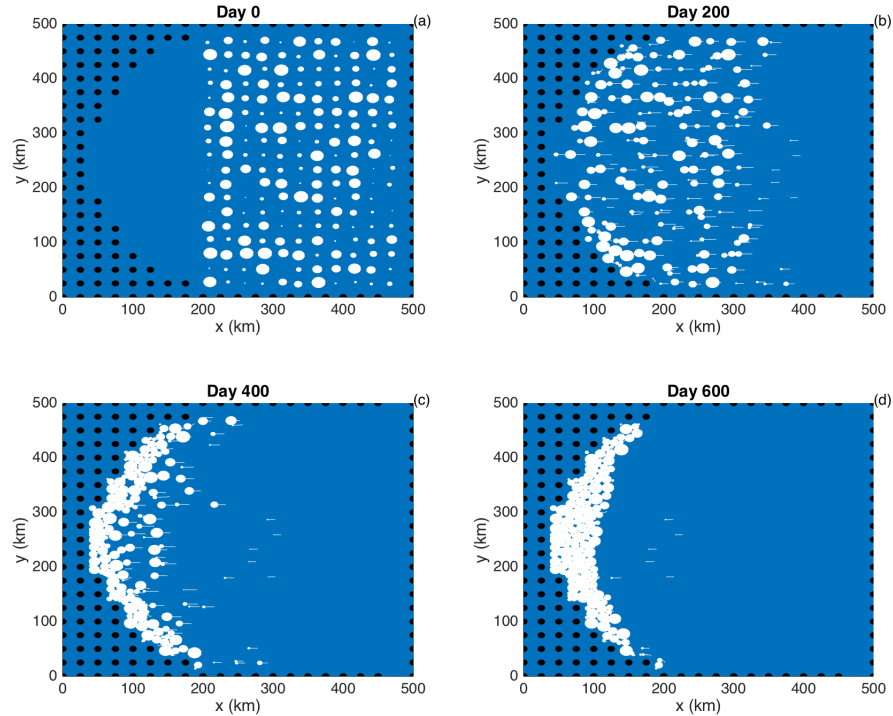
906 **Figure 1.** Schematic showing how Lagrangian elements are used when modeling tabular icebergs. La-  
 907 grangian elements (blue dots) are initialized in a staggered lattice covering the surface area of the iceberg.  
 908 For purposes of mass aggregation, the ice elements are assumed to have hexagonal shape (grey hexagons).  
 909 For purposes of element interactions, the ice elements are assumed to be circular (black circles). Elements  
 910 are initially bonded to adjacent elements using numerical bonds (dashed white lines). These numerical bonds  
 911 form equilateral triangles which give the shape rigidity. The inset panel shows a schematic of the intersection  
 912 of a hexagonal element and the ocean grid. The colors indicate the fraction of the hexagon that lies in each  
 913 grid cell. These fractions are used as weights to spread LBIM properties to the ocean grid (see text for more  
 914 details) The background photo in the larger schematic is an areal photograph of iceberg PIIB (Area= 42 km<sup>2</sup>)  
 915 taken in Baffin Bay in 2012. The red ship can be identified on the bottom of the photo for scale.



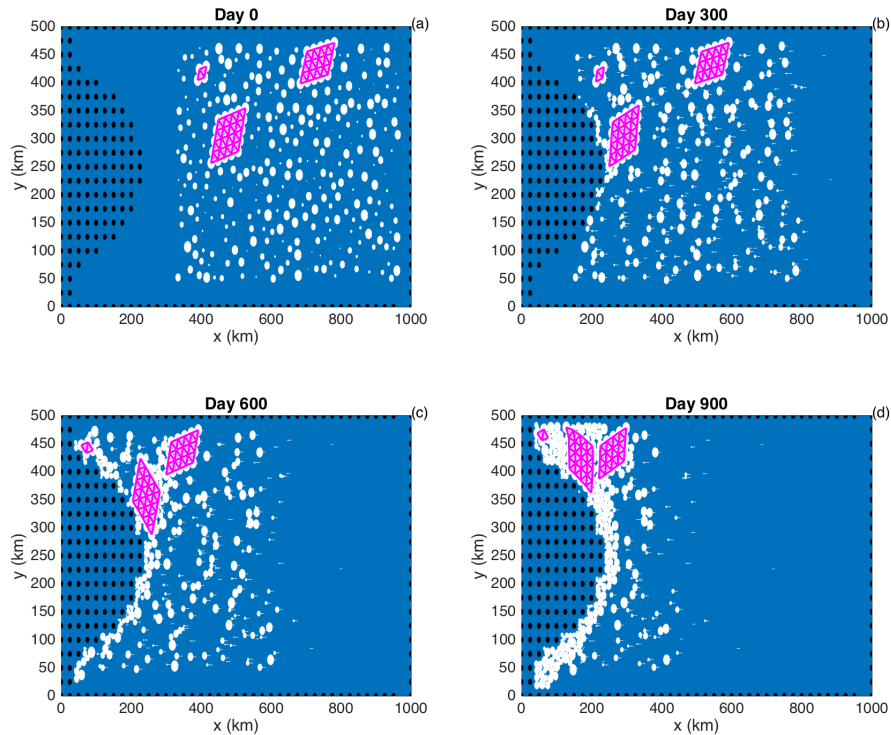
916 **Figure 2.** Snapshots of the fraction of ice cover in the LBIM tabular iceberg calving simulation. Snapshots  
917 are taken (a) 7, (b) 15, and (c) 30 days after calving. The dashed line in panel (c) shows the location of the  
918 vertical transects shown in Figures 8 and 7.



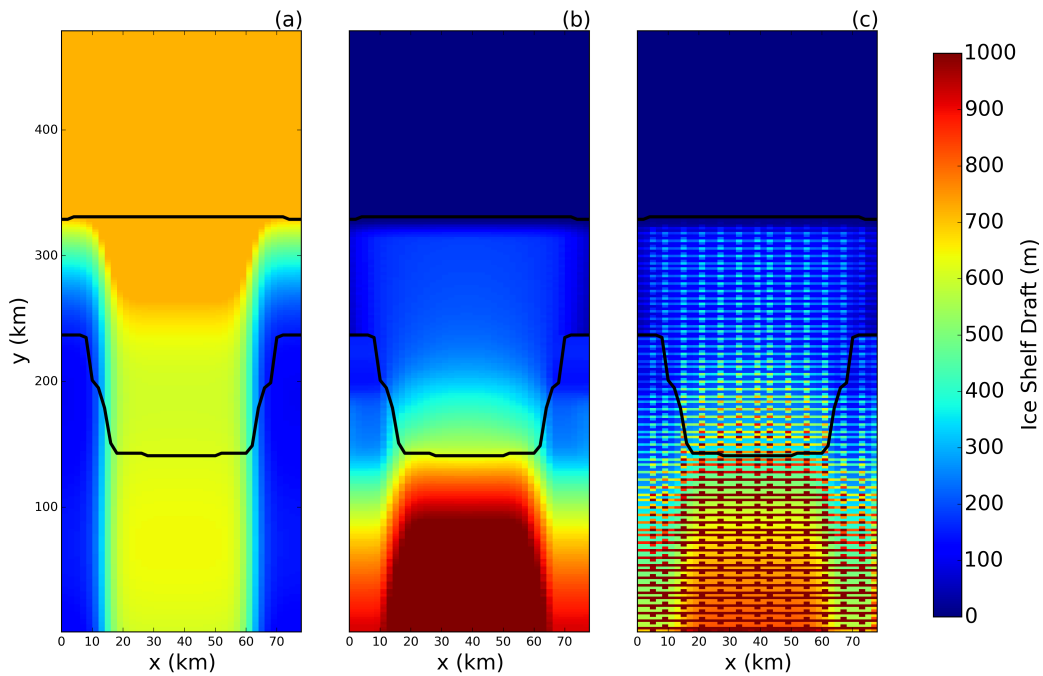
919 **Figure 3.** Snapshots of the sea surface temperature in the LBIM tabular iceberg calving simulation. Snap-  
920 shots are taken (a) 7, (b) 15, and (c) 30 days after calving. Regions with ice area fraction = 1 area plotted in  
921 white.



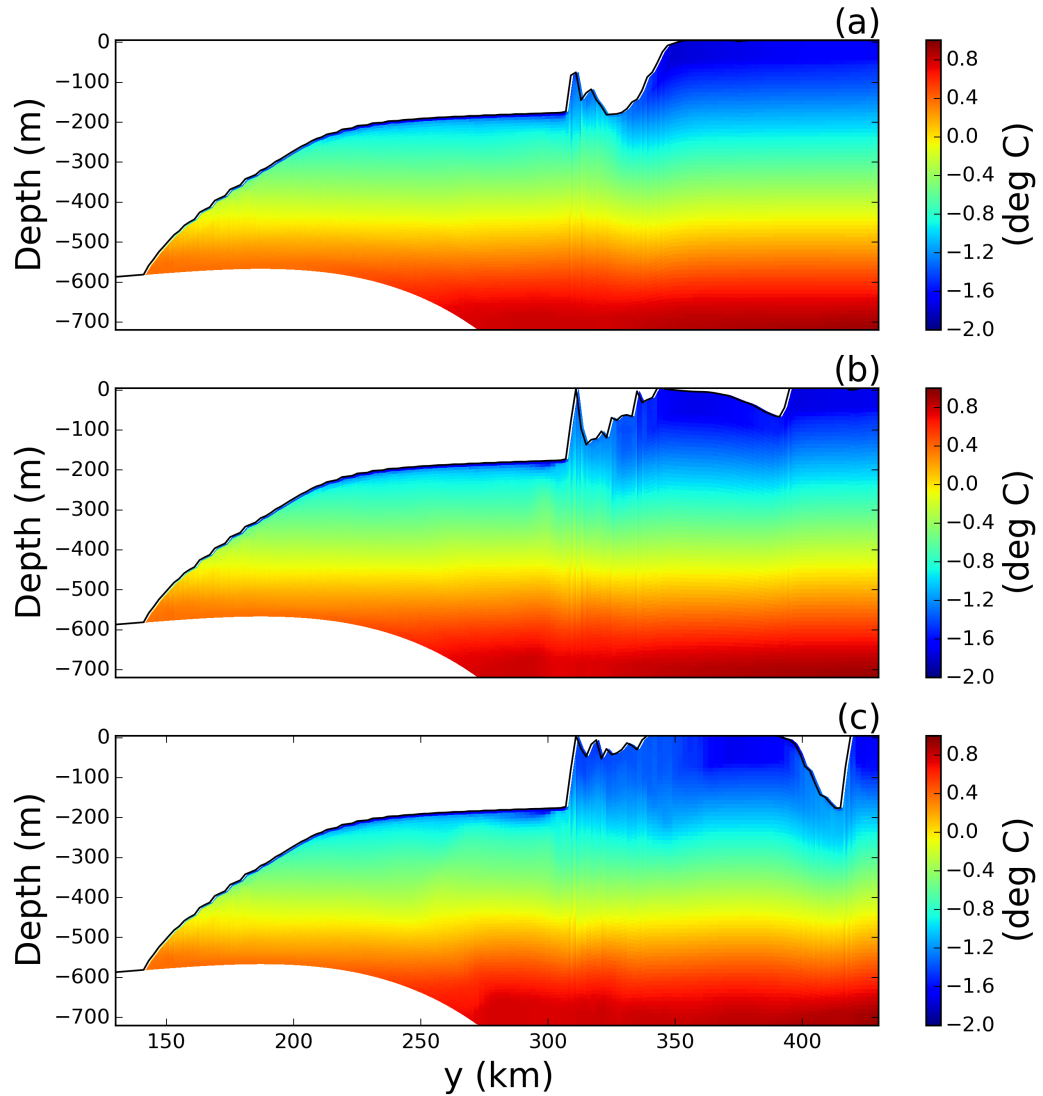
922 **Figure 4.** Results of an ice-only LBIM simulation with no bonds between ice elements. Ice elements are  
 923 initialized throughout the domain, as shown in panel (a). The elements are forced by an imposed westward  
 924 ocean current of  $u=0.1\text{m/s}$  (no ocean model is used). Forces due to sea surface slope, atmospheric drag, Cori-  
 925 olis and sea ice drag are set to zero. The figure shows snapshots of ice element positions at time (a)  $t=0$ , (b)  
 926 200, (c) 400, (d) 600 days. The size of the dots shows the surface area (and interaction diameter) of each ice  
 927 element. The white tails behind the elements show the elements' positions over the preceding two days. Land  
 928 points are shown by black circles.



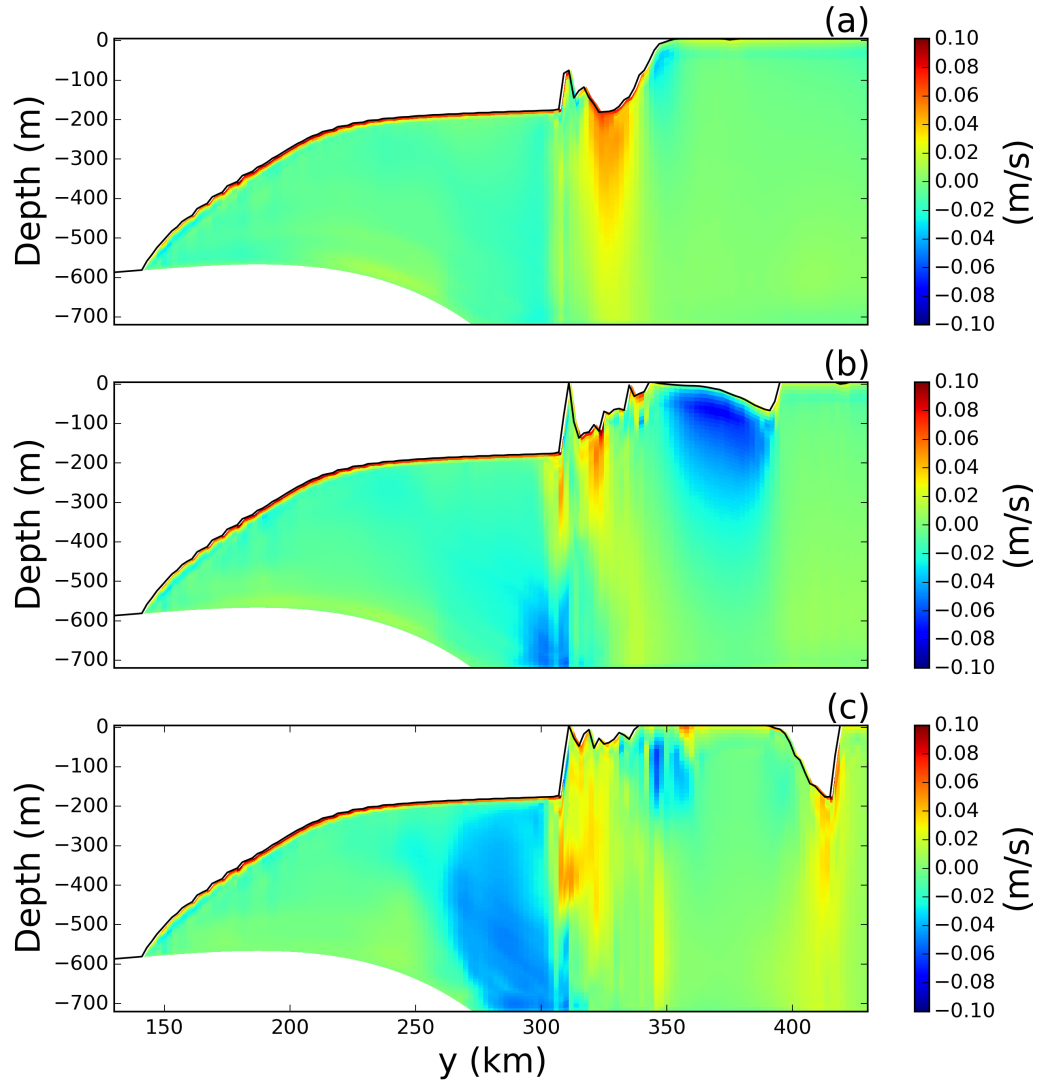
929 **Figure 5.** Results of an ice-only LBIM simulation using bonds between elements. Ice elements are ini-  
 930 tialized throughout the domain, as shown in panel (a). Three tabular icebergs are included, with 25, 16 and 4  
 931 elements respectively. The elements are forced by an imposed westward ocean current of  $u=0.1\text{m/s}$  (no ocean  
 932 model is used). Forces due to sea surface slope, atmospheric drag, Coriolis and sea ice drag are set to zero.  
 933 The figure shows snapshots of ice element positions at time (a)  $t=0$ , (b) 300, (c) 600, (d) 900 days. The size  
 934 of the dots shows the surface area (and interaction diameter) of each ice element. The white tails behind the  
 935 elements show the elements' positions over the preceding two days. Bonds between ice elements are plotted  
 936 in magenta. Land points are shown by black circles.



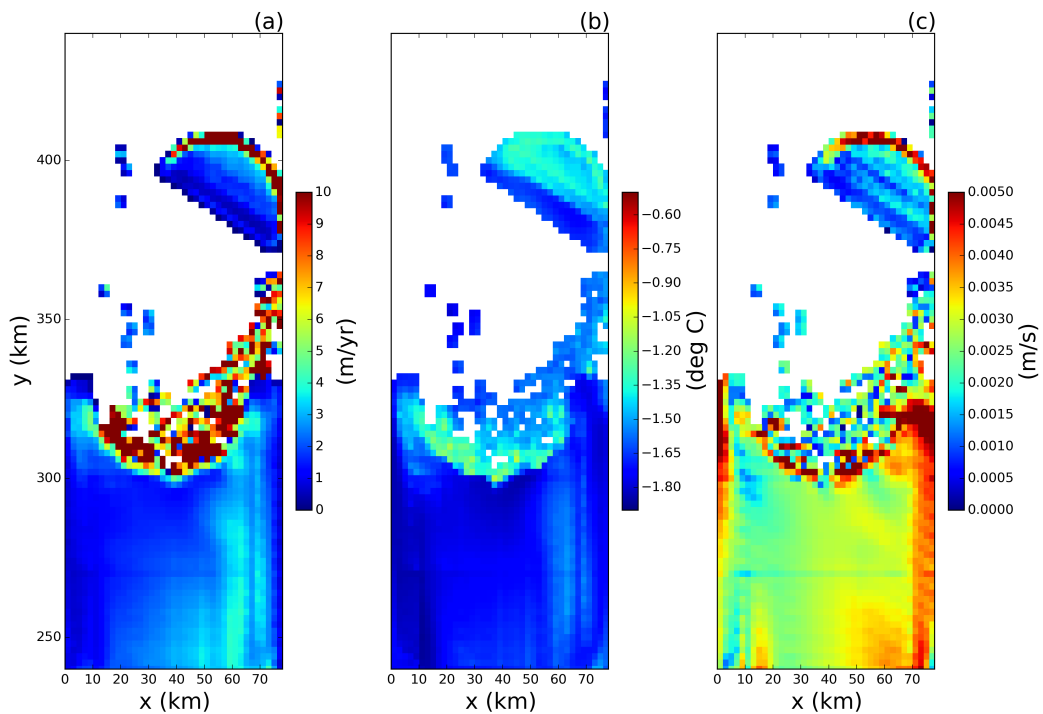
937 **Figure 6.** (a) Ocean bottom topography and (b) ice-shelf draft used to initialized the tabular iceberg calv-  
 938 ing simulation. The ice draft is calculated from the total mass in an ocean grid cell after the mass-spreading  
 939 interpolation has been applied (as explained in Section 2.3). (c) Initial ice draft that would be calculated if the  
 940 mass-spreading interpolation were not used (i.e.: elements treated as point masses).



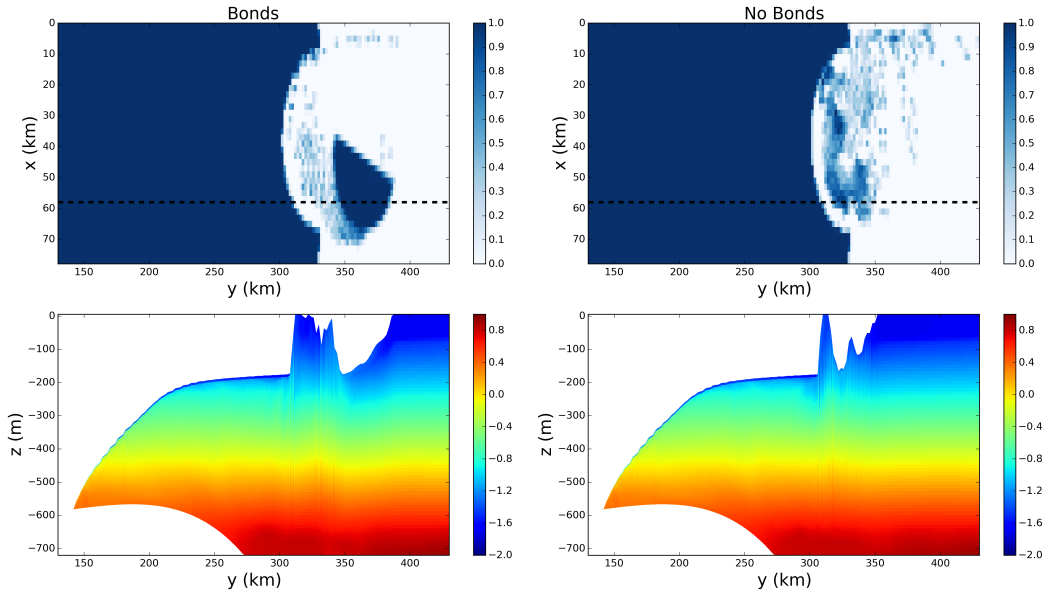
941 **Figure 7.** Snapshots of vertical sections of ocean temperature at  $x = 58$  km in the LBIM tabular iceberg  
 942 calving experiment. Snapshots are taken (a) 7, (b) 15, and (c) 30 days after calving. The position of the  
 943 vertical transects is shown by the dashed lines in Figure 2c.



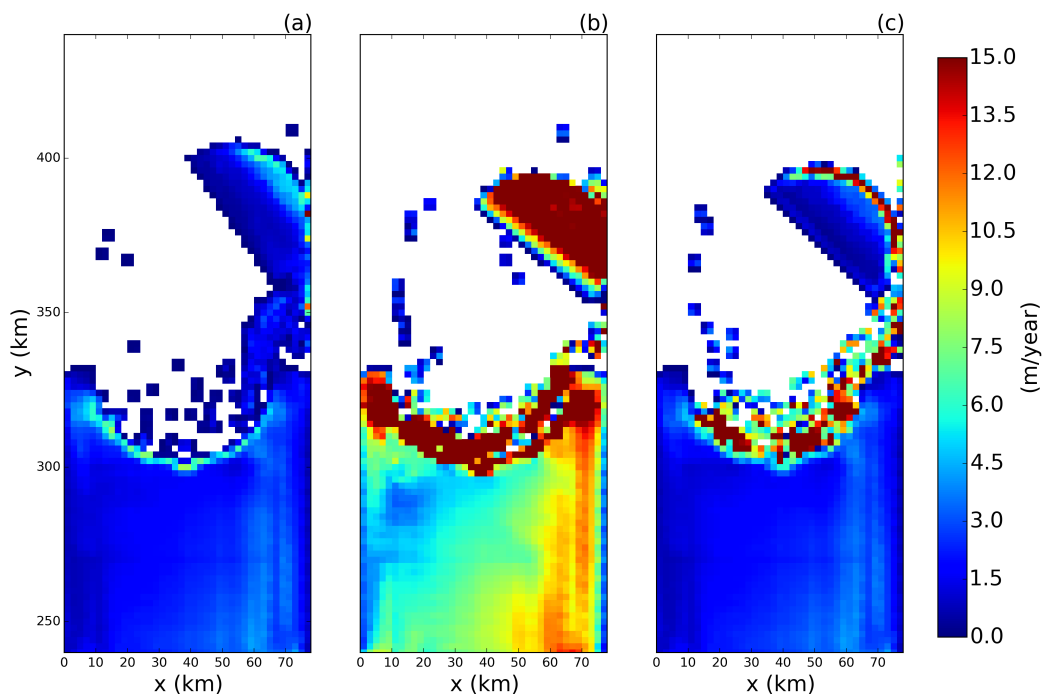
944 **Figure 8.** Snapshots of vertical sections of meridional velocity at  $x = 58$  km in the LBIM tabular ice-  
 945 berg calving simulation. Snapshots are taken (a) 7, (b) 15, and (c) 30 days after calving. The position of the  
 946 transects is shown by the dashed line in Figure 2c.



947 **Figure 9.** Results of the tabular iceberg calving simulation 30 days after the iceberg calves. The three panels  
 948 show snapshots of the (a) melt rate, (b) top-of-ocean temperature and (c)  $u^*$  at the base of the ice shelf.  
 949 Fields are only shown in regions where the ice area fraction is  $\geq 0.8$ .



950      **Figure 10.** Results from the tabular iceberg calving experiment with and without iceberg bonds. The top  
 951      row shows the fractional ice cover for the simulations (a) with and (b) without numerical bonds. The bottom  
 952      row shows the corresponding vertical temperature section at  $x = 58$  km for the simulation (c) with and (d)  
 953      without bonds. The location of the vertical transects in panels (c) and (d) are shown by the dashed lines in  
 954      panels (a) and (b), respectively. All snapshots are taken at time  $t = 30$  days. The simulations use wind stress  
 955       $\vec{\tau} = <0.0, 0.05>$ .



956 **Figure 11.** Melt rate 30 days after calving for simulations using (a) three equation  
957 model, (b) icebergs drift parametrization, (c) a mixture between the two (as described in Section 2.5.)

958      **9 Supplementary Material**

959      The experiment configuration used to initialize the calving tabular iceberg simulation  
960      (in this study) is the same as that of the Ocean0 setup in the MISOMIP, with the follow-  
961      ing three changes made:

- 962      1. The ‘calving criteria’ used in the MISOMIP study (which states that all points in  
963      the ice shelf with thickness less than 100m are set to zero thickness) has not been  
964      used.
- 965      2. The ice shelf has been thickened on the flanks of the domain, so that the latitude of  
966      the grounding line increases away from the center of the ice shelf.
- 967      3. The ice shelf is configured to be symmetric about its meridional center line ( $x =$   
968       $\frac{L_x}{2}$ ). This was achieved by using the average of the left and right flanks of the ice-  
969      shelf thickness.

970      These three changes were made in order to make the circulation beneath the ice shelf eas-  
971      ier to interpret.